Natural Resources Canada | Ressources naturelles Canada

GEOLOGICAL SURVEY OF CANADA
OPEN FILE 8062

Ripley Landslide: the geophysical properties of a slow-moving landslide near Ashcroft, British Columbia

**D. Huntley, P. Bobrowsky,
N. Parry, P. Bauman, C. Candy, and M. Best**

2017

GEOLOGICAL SURVEY OF CANADA
OPEN FILE 8062

Ripley Landslide: the geophysical properties of a slow-moving landslide near Ashcroft, British Columbia

D. Huntley[1], P. Bobrowsky[2], N. Parry[3], P. Bauman[4], C. Candy[5], and M. Best[6]

1. Geological Survey of Canada, 1500-605 Robson Street, Vancouver, British Columbia
2. Geological Survey of Canada, 9860 West Saanich Road, Sidney, British Columbia
3. Tetra Tech EBA Inc., 14940-123 Avenue NW, Edmonton, Alberta
4. Advisian-Worley Parsons Group, 500-151 Olympic Road SW, Calgary, Alberta
5. Frontier Geosciences Inc., 237 St. Georges Avenue, North Vancouver, British Columbia
6. Bemex Consulting International, 3107 Wild Berry Bend, Victoria, British Columbia

2017

doi:10.4095/300563

Recommended citation
Huntley, D., Bobrowsky, P., Parry, N., Bauman, P., Candy, C., and Best, M., 2017. Ripley Landslide: the geophysical properties of a slow-moving landslide near Ashcroft, British Columbia; Geological Survey of Canada, Open File 8062, 66 p. doi:10.4095/300563

Publications in this series have not been edited; they are peer reviewed and released as submitted by the author.

Ripley Landslide: the geophysical properties of a slow-moving landslide near Ashcroft, British Columbia, Canada

Huntley, D.[1], Bobrowsky, P.[2], Parry, N.[3], Bauman, P.[4], Candy, C.[5] and Best, M.[6]

1. Geological Survey of Canada, Vancouver, British Columbia
2. Geological Survey of Canada, Sidney, British Columbia
3. TetraTech EBA Inc., Edmonton, Alberta
4. Advisian, Worley Parsons Group, Calgary, Alberta
5. Frontier Geosciences Inc., North Vancouver, British Columbia
6. BEMEX Consulting International, Victoria, British Columbia

Corresponding author: david.huntley@canada.ca

Abstract

Landslide hazards in the Thompson River valley, British Columbia adversely impact vital national railway infrastructure and operations, the environment, cultural heritage features, communities, public safety and the economy. Field investigations and monitoring of the very slow-moving Ripley Landslide, 7 km south of Ashcroft, indicates movement across the main body, with the greater displacement at the south end of the slide near a lock-block retaining wall separating Canadian National (CN) and Canadian Pacific (CPR) rail tracks. Knowledge of the internal composition and structure of the landslide as interpreted through surficial geology mapping and geophysical surveys provide contextual baseline data for interpreting monitoring results and understanding mass-wasting processes in the Thompson River transportation corridor. Bathymetry measurements, electrical resistivity tomography, frequency-domain electromagnetic terrain conductivity, ground penetrating radar, seismic refraction, multi-spectral surface wave analyses, and borehole logging of natural gamma, conductivity and magnetic susceptibility all suggest a moderately high relief bedrock sub-surface overlain by a >20 m thick package of clay, silt, till diamicton and gravel. Planar physical sub-surface features revealed in field observations, geophysical profiles and borehole logs include tabular bedding and terrain unit contacts, in addition to curvilinear-rectilinear features interpreted as sub-horizontal rotational-translational slide surfaces in clay-rich beds beneath the rail ballast and retaining wall at depths between 5 m and 15 m below the surface of the main landslide body. Geophysical data presented support field observations and borehole logs that show sub-surface glaciolacustrine unit boundaries are gradational rather than sharply defined. Geophysical profiles show that clay-rich glacial deposits are the units most likely to contain failure planes. The landslide toe extends under the Thompson River where clay-rich sediments are confined to a >20 m deep bedrock basin. The upper clay beds are armoured from erosion by a lag deposit of modern fluvial boulders except along the west river bank where a deep trough has been carved by strong currents. Waterborne conductivity measurements indicate groundwater discharge at three zones across the submerged landslide toe. Fluvial incision of the submerged toe slope at the south end of the landslide is observed <50 m west of where critical railway infrastructure is at risk. Integrating data from surficial geology mapping and an array of geophysical techniques provided significantly more information than any one method on its own.

Keywords
Landslide, Ashcroft, British Columbia, Canadian National Railway, Canadian Pacific Railway, Surficial Geology Mapping, Geophysical Surveys, Electrical Resistivity Tomography, Fixed Frequency Electromagnetic Terrain Conductivity, Ground Penetrating Radar, Seismic Refraction, Multi-Spectral Surface Wave Analysis, Borehole Conductivity, Natural Gamma, Magnetic Susceptibility

Table of Contents

Page

Open File Title and Authors……..…… 1
Citation and Copyright…….…….…… 2
Title……..…… 3
Abstract…….……. 3
Keywords……...… 4

1. Introduction…….…….. 7

1.1 Landslide Geohazards in the Thompson River Valley……...…….... 7
1.2 Ripley Landslide and Railway Infrastructure at Risk……...…..……. 9
1.3 Landslide Mapping and Monitoring at the Ripley Landslide……...……. 9
1.4 Ripley Landslide: Knowledge Gaps in Landslide Composition and Geophysical Survey Objectives…….……. 12

2. Terrestrial and Waterborne Geophysical Survey Methods…..…….. 14

2.1 Terrestrial Geophysics Campaign……...…… 16
2.1.1 Terrestrial Electrical Resistivity Tomography (T-ERT)……...…... 16
2.1.2 Terrestrial Fixed Frequency Electromagnetic Induction (T-FEM)……..…….. 18
2.1.3 Terrestrial Ground Penetrating Radar (T-GPR)……..... 18
2.1.4 Terrestrial Seismic Refraction Survey (SR)……..….. 19
2.1.5 Terrestrial Multi-Spectral Analysis of Surface Waves (MASW)……..... 20

2.2 Waterborne Geophysics Campaign……..…..…. 21
2.2.1 Acoustic Bathymetry (AB)……..……. 21
2.2.2 Waterborne Electrical Resistivity Tomography (W-ERT)……... 21
2.2.3 Waterborne Electromagnetic Induction Methodology (W-EM31)……...…… 22
2.2.4 Waterborne Ground Penetrating Radar (W-GPR)……...…... 22

2.3 Borehole Geophysics Campaign……...….. 23
2.3.1 Borehole Geophysical Survey (GR, EM and MS)……...…. 23

3. Terrestrial Geophysics Results and Interpretation…….. 25

3.1 Interpretation of Terrestrial Electric Resistivity Tomography Results……...… 25
3.2 Interpretation of Terrestrial Electromagnetic Induction Results……. 31
3.3 Interpretation Terrestrial Ground Penetrating Radar Results…….. 34
3.4 Interpretation of Terrestrial Seismic Refraction Results……..….... 35

3.5 Interpretation of Terrestrial Multispectral Analysis of Shear Wave Results…..... 39

4. Waterborne Geophysics Results and Interpretation……...…. 42

4.1 Interpretation of Acoustic Bathymetry Results……...… 42
4.2 Interpretation of Waterborne Electrical Resistivity Tomography Results…..…..... 43
4.3 Interpretation of Waterborne Electromagnetic Induction Results……...…... 44
4.4 Interpretation of Waterborne Ground Penetrating Radar Results……...…… 45

5. Borehole Geophysics Results and Interpretation……..….. 50

5.1 Interpretation of Borehole Geophysics Results……...…… 51

6. Discussion and Summary: Addressing Knowledge Gaps……. 56

6.1 Logistics, Constraints and Limitations……. 56
6.2 Outcome of the Multi-Technique Approach…… 56
6.3 Landslide Geophysical Model…….. 57
6.4 Recommendations for Future Work and Summary……...……... 59

7. Acknowledgements……. 63

8. References……. 64

1. Introduction

Landslides in the mountain valleys of western Canada have challenged the development and operation of railways since the late 19th Century. In the 21st Century, pronounced economic and environmental repercussions can occur when rail service is disrupted by landslide activity. A vital section of the national railway transportation corridor runs through the Thompson River valley in southern British Columbia. This is a unique area where complex glacial geology, active geomorphic processes and rail infrastructure intersect and have been affected by slope instability for many decades (**Figure 1a**).

To better understand and manage landslide geohazards along this section of the railway corridor, an international multi-year project is investigating and monitoring the Ripley Landslide, approximately seven kilometres south of Ashcroft, B.C. (**Figure 1b, c**). This small, very slow moving landslide is adversely impacting railway infrastructure and operation (Bunce and Chadwick, 2012; Bobrowsky et al., 2014). Here, we address significant knowledge gaps in the nature and distribution of subsurface materials, their stratigraphic relationships and internal structure of the landslide through the application of a suite of geophysical techniques. Results of the geophysical surveys discussed in this report provide contextual base-line data for interpreting results from other aspects of the project (e.g., Huntley and Bobrowsky, 2014; Huntley et al., 2014; Macciotta et al., 2014; Hendry et al., 2015; Schafer et al. 2015).

1.1 Landslide Geohazards in the Thompson River Valley

In the Thompson River valley, B.C., landslides are confined to multiple glaciolacustrine clay-rich units, boulder-rich till diamictons, and outwash sand and gravel related to at least three Pleistocene glaciations (Fulton, 1969; Ryder, 1976; Ryder et al. 1991; Clague and Evans 2003; Johnsen and Brennand 2004; Tribe 2005; Eshraghian et al., 2007). Landslides include: (1) slow-moving (2 cm to 10 cm/yr) rotational failures with large back-tilted blocks; (2) slow-moving (2 cm to 10 cm/yr) retrogressive translational slides with little rotation; and (3) rapid debris slumps involving flowage and sliding of landslide material (Clague and Evans, 2003). Large rotational and retrogressive translational landslides were initially triggered through deep incision of Pleistocene valley fill by post-glacial Thompson River. Although some landslides failed and moved rapidly in prehistoric times, in recent times, all are slow-moving reactivated compound features. For most, movement occurs along weak, sub-horizontal glaciolacustrine zones confined between overlying till and underlying gravel deposits and bedrock (Monger and McMillan, 1984; Monger, 1985; Mortimer, 1987; Porter et al., 2002; Clague and Evans, 2003; Bishop et al., 2008; Eshraghian et al., 2007; 2008; Bunce and Chadwick, 2012). The Thompson River affects landslide stability by: (1) changing pore water pressure in the slope mass and along rupture surfaces; (2) altering supporting force on landslide toes during seasonal changes in river discharge; and (3) through cut-bank erosion affecting landslide geometry (Clague and Evans, 2003; Eshraghian et al., 2007; 2008; Hendry et al., 2015).

There are three strategies for government agencies and railway companies to reduce the risks associated with landslides in the Thompson River rail transportation corridor: (1) avoid landslide-prone terrain – not possible for either Canadian National (CN) and Canadian Pacific (CPR) tracks

in the valley; (2) stabilizing landslides – prohibitively costly geotechnical problems preclude this option; and (3) identifying landslide-prone terrain and monitoring for unsafe ground movement – the most cost effective risk management approach for railway companies and government agencies (Bunce and Chadwick, 2012). To this end, an international consortium of research partners has embarked upon a detailed multi-year study to investigate and monitor an active landslide in a collective effort to better understand and manage the Ripley Landslide and, by extension, other landslide hazards in Canada and elsewhere (Bobrowsky et al., 2014).

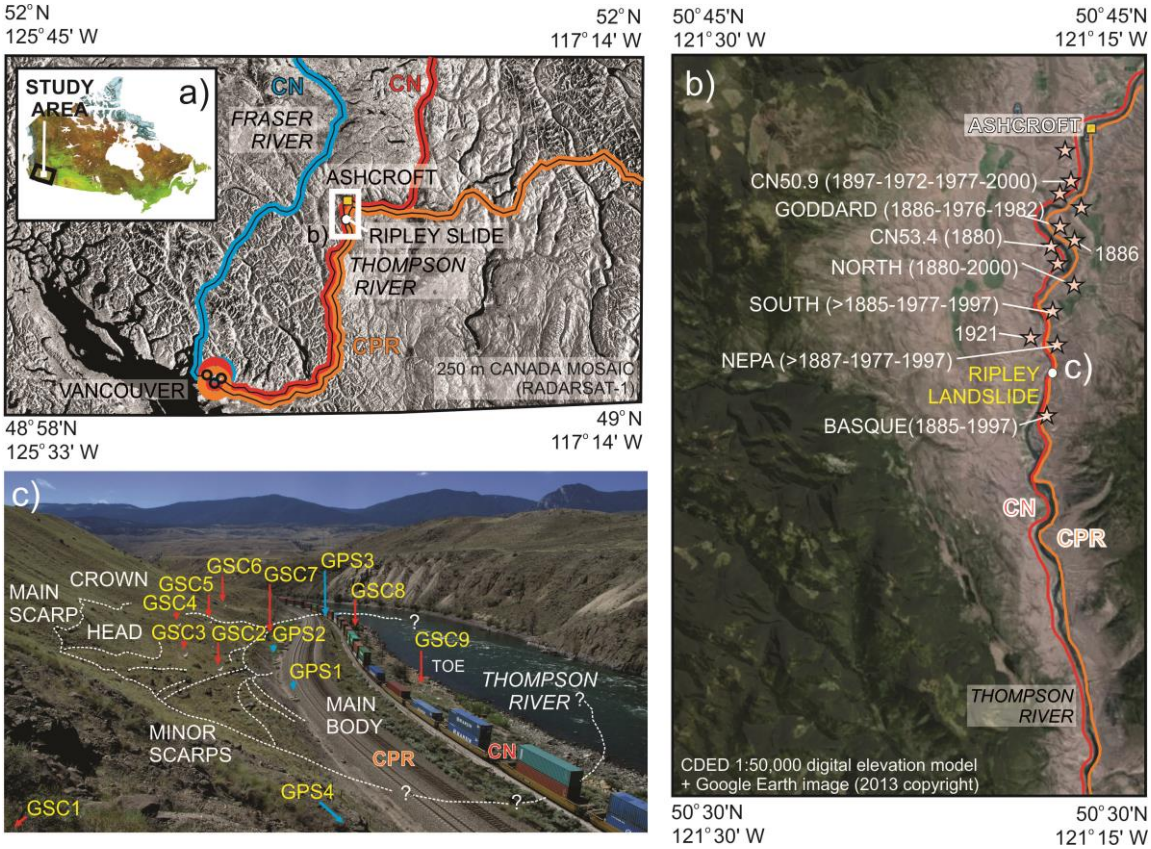

Figure 1 a) Rail transportation corridors in southwestern British Columbia with location of study area; b) Landslides of the Thompson River valley rail transportation corridor with location of Ashcroft and the Ripley Landslide; c) Overview of the Ripley Landslide highlighting the location of GPS monitoring stations (GPS1-4) and InSAR corner reflectors (GSC1-9); fiber optic monitoring systems are installed along the retaining wall separating the CN and CPR tracks; maximum displacement of the landslide occurs at GPS3; view to south.

1.2 Ripley Landslide and Railway Infrastructure at Risk

The Ripley Landslide, located 7 km south of Ashcroft, B.C. (**Figure 1b**), is approximately 220 m long (N-S) by 150 m wide (E-W), with an estimated volume of 400,000 m^3. The landslide has been active since 1951; and although movement was slow through the late Twentieth Century, cumulatively it was sufficient to open numerous tension cracks in the main body of the landslide and cause a visible displacement in the fence line east of the tracks by the early 2000s (Bunce and Chadwick, 2012). In 2005, a rail siding was extended across the landslide that required upslope cuts and embankment widening, including the construction of a lock-block retaining wall

separating the CN and CPR tracks at the southwest limit of the toe slope (**Figure 2**). During the autumn of 2006 and spring of 2007, track lifting between 10 mm to 20 mm as often as every three to six weeks was required; and a back scarp of a 40,000 m^3 portion of the landslide became visible in the excavated cut slope (**Figure 2**). Tracks are lifted and ballast is added when needed during the year to accommodate lateral and vertical displacement across the main body of the slide. Sagging is also observed in the lock-block retaining wall.

The landslide is a significant hazard to the onsite infrastructure since both CN and CPR tracks run adjacent to each other along the entire breadth and beyond the limits of the Ripley Landslide. On average some 80 trains per 24 hour period travel through the area, crossing this unstable landform. Locomotives traverse the landslide at a precautionary maximum speed of 30 km/hr; so in the event of a derailment, the potential is low for injury and death of individuals on board. Potential environmental damage to Thompson River and groundwater by spilled dangerous goods is also minimized at this speed (Bunce and Chadwick 2012). Unfortunately, as the magnitude and frequency of landslide activity increases, the frequency of track maintenance and operation costs rise. Consequently, the environmental and economic repercussions of a severed railway here remain pronounced.

1.3 Mapping and Monitoring at the Ripley Landslide

Surficial geology mapping and stratigraphic logging has established that the Ripley Landslide involves the following earth materials: deeply eroded Mesozoic bedrock; Pleistocene colluvium, glaciolacustrine sediments, till, glaciofluvial sediments; and Holocene colluvial deposits, alluvial sediments and anthropogenic fill (e.g., railway ballast, culverts) (Huntley and Bobrowsky, 2014; Hendry et al., 2015). At the surface, the dominant earth materials exposed on the landslide are colluvial, fluvial and anthropogenic units (**Figure 2a**). Borehole logs show that beneath these surface units lie Fraser Glaciation deposits in-filling a pre-Late Wisconsinan bedrock paleovalley depression to a maximum depth of 32 m below the landslide surface (**Figure 2b**).

An extensive array of innovative monitoring technologies have now been installed and are monitoring activity across the landslide (**Figure 1c**, **Figure 2a**), including: permanent global positioning stations (Bunce and Chadwick, 2012); piezometers and ShapeAccelArray inclinometry in observation wells (Macciotta et al., 2014); fiber Bragg grating (FBG) and Brillouin optical time domain reflectometry (BOTDR) networks on the retaining wall (Bobrowsky et al., 2014); and InSAR corner reflectors for RADARSAT-2 interferometry and ground-based SAR and LiDAR (Huntley et al., 2014; Macciotta et al., 2014). These monitoring systems have been installed to understand the deformation mechanisms and potential triggers for sudden movement at the Ripley Landslide (Huntley et al., 2014; Macciotta et al., 2014; Schafer et al., 2015), and to help manage the risks associated with railway operations (Bunce and Chadwick, 2012).

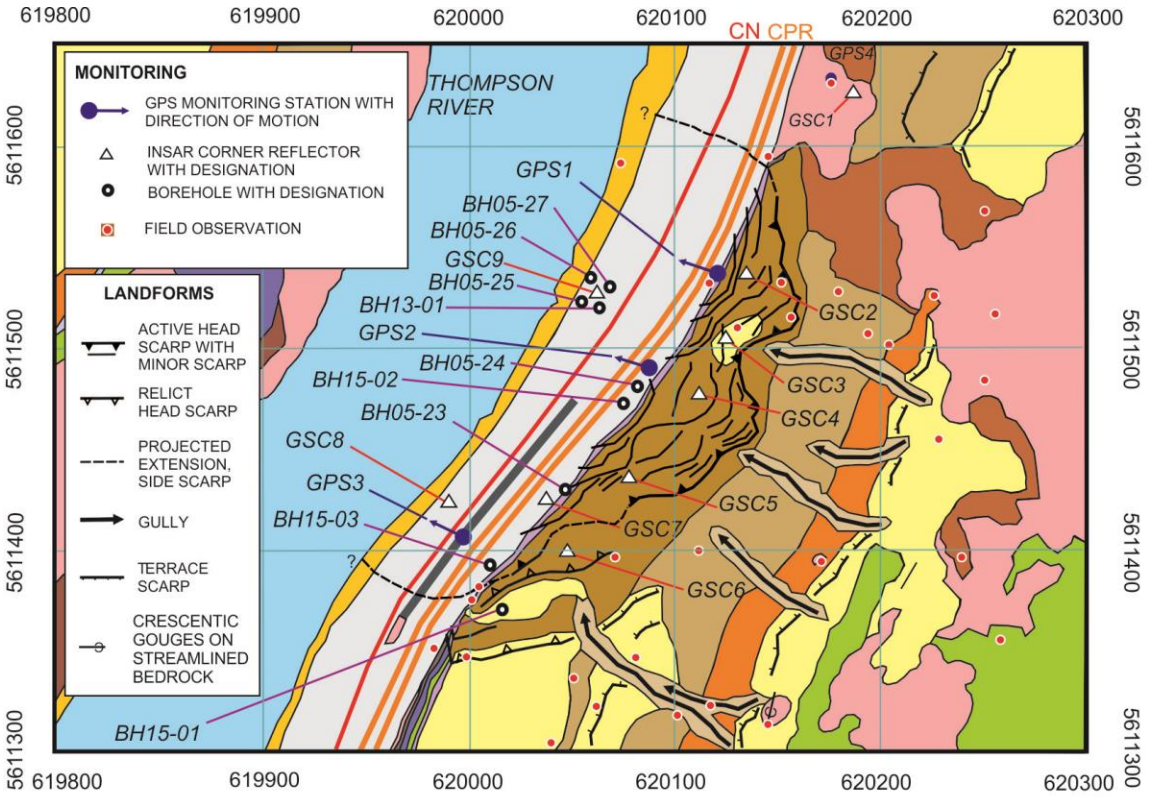

SURFICIAL DEPOSITS

ANTHROPOCENE

H — **UNIT 10 - ANTHROPOGENIC MATERIALS:** RAIL BALLAST, TRAIN TRACKS, CULVERTS, LOCK-BLOCKS (CANADIAN PACIFIC AND CANADIAN NATIONAL)

HOLOCENE

Ap — **UNIT 9 - ALLUVIAL FLOODPLAIN DEPOSITS:** BOULDERS, GRAVEL AND SAND

Cv — **UNIT 8 - COLLUVIAL VENEER:** SILT, SAND, COBBLES AND BOULDERS; GLACIOFLUVIAL OUTWASH REWORKED BY SOIL CREEP, HILLSLOPE WASH AND GULLY EROSION

Cv — **UNIT 8 - COLLUVIAL VENEER:** SILT, SAND, COBBLES AND BOULDERS REWORKED BY SOIL CREEP, HILLSLOPE WASH, DEBRIS FLOWS AND GULLY EROSION; OVERLYING TILL AND GLACIOLACUSTRINE DEPOSITS

Cv — **UNIT 8 - COLLUVIAL VENEER:** CLAST-SUPPORTED COBBLES AND BOULDERS DERIVED FROM BEDROCK BY ROCK FALL AND DEBRIS FALL; REWORKED BY SOIL CREEP, DEBRIS FLOW AND GULLY EROSION

Cb — **UNIT 8 - COLLUVIAL BLANKET:** STRATIFIED, CLAST-SUPPORTED SILT AND SAND-RICH DIAMICTON; TILL AND GLACIOLACUSTRINE DEPOSITS REWORKED BY SOIL CREEP, DEBRIS FLOW AND GULLY EROSION

Af — **UNIT 7 - ALLUVIAL FAN DEPOSITS:** CLAY, SILT AND SAND DRAPED OVER BEDROCK, TILL AND GLACIOFLUVIAL SEDIMENTS

LATE PLEISTOCENE (LATE WISCONSINAN)

GFt — **UNIT 6 - GLACIOFLUVIAL DEPOSITS:** RETREAT PHASE GRAVEL AND SAND OUTWASH; TERRACED

GLvb — **UNIT 5 - GLACIOLACUSTRINE DEPOSITS:** INTERBEDDED SILT, SAND, CLAY, GRAVEL AND DIAMICTON; MEDIUM TO HIGHLY PLASTIC

Tvb — **UNIT 4 - TILL DEPOSITS:** MASSIVE DIAMICTON WITH SAND AND SILT MATRIX; ABUNDANT ERRATIC BOULDERS AT SURFACE AND DEPTH

GLb — **UNIT 3 - GLACIOLACUSTRINE DEPOSITS:** INTERBEDDED CLAY, SILT, SAND AND DIAMICTON; MEDIUM TO HIGHLY PLASTIC

Cvb — **UNIT 2 - COLLUVIAL DEPOSITS:** CLAST-SUPPORTED COBBLES AND BOULDERS DERIVED FROM BEDROCK BY ROCK FALL; AND SILT AND CLAY MATRIX-SUPPORTED STRATIFIED DIAMICTONS DEPOSITED BY DEBRIS FLOW IN A GLACIAL LAKE

Bedrock

R — **UNIT 1 - BEDROCK:** ANDESITE, RHYOLITE AND VOLCANICLASTIC ROCKS; FRACTURED, JOINTED AND FAULTED

Figure 2a Surficial geology and landforms of the Ripley Landslide and adjacent terrain; location of GPS monitoring stations (GPS1-4) InSAR corner reflectors (GSC1-9) and boreholes (BH05-23 to BH05-27, BH13-01, BH15-01 to BH15 03 – see **Figure 2b** and **Figure 15a-c**). The units described in the map legend will be referred to in the following interpretations and discussion of geophysical results (modified from Huntley and Bobrowsky, 2014).

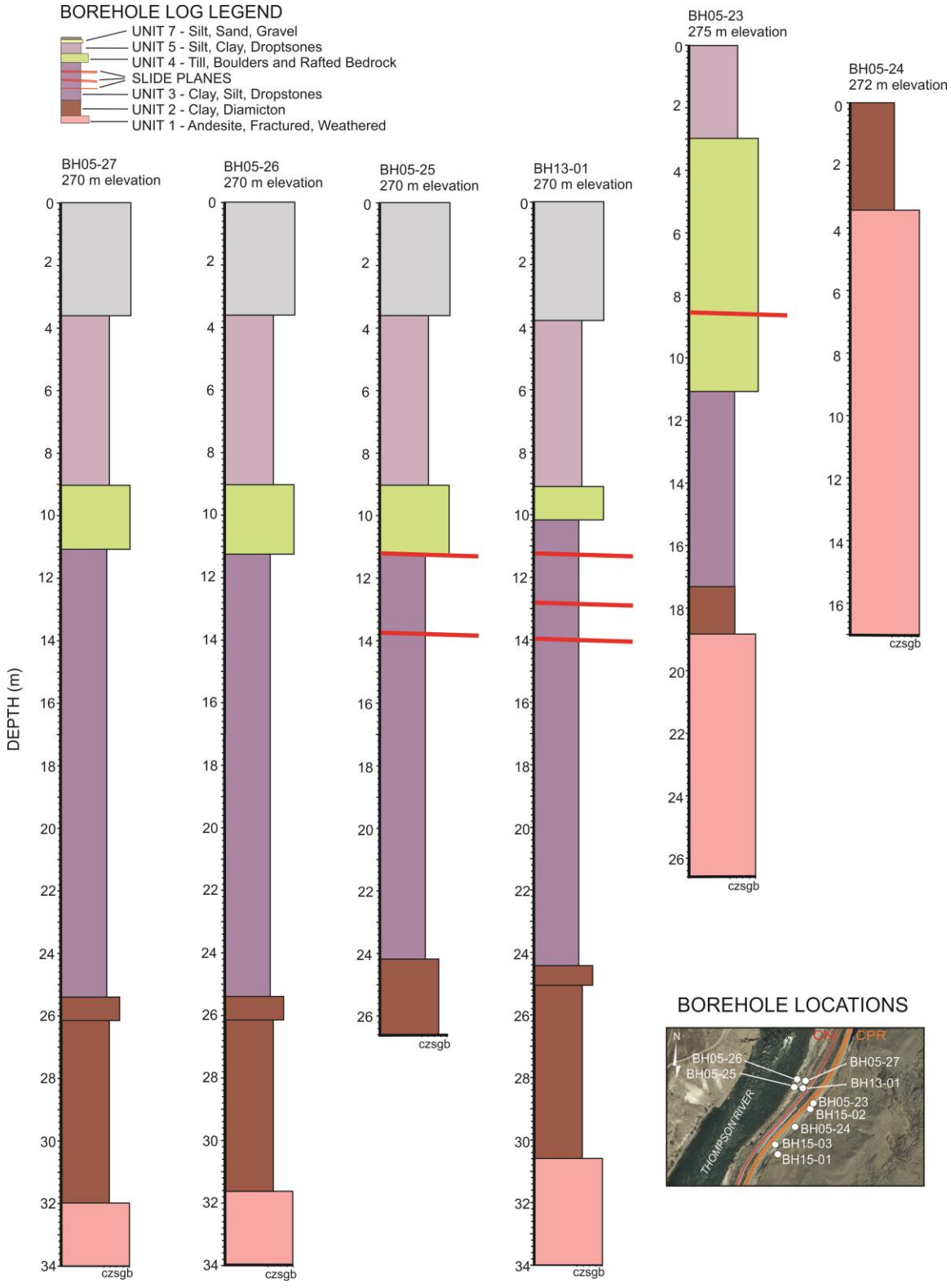

Figure 2b Boreholes drilled for CN and CPR at the Ripley Landslide from 2005 to 2015(BH05-23 to BH05-27, BH13-01; BH15-01 to BH15-03). Surficial geology based upon interpretations of geotechnical logs (BGC, 2005; BGC, 2013; and this study) and field observations of earth materials, lithological content and stratigraphic order (Huntley and Bobrowsky, 2014).

Similar to other mass movements in the Thompson River valley (**Figure 1b**), the Ripley Landslide is a very slow-moving reactivated compound feature, in which displacement occurs along weak, sub-horizontal zones in glaciolacustrine clay-rich beds confined between overlying till and underlying gravel deposits and bedrock (Porter et al., 2002; Clague and Evans, 2003; Bishop et al., 2008; Eshraghian et al., 2007; 2008; Bunce and Chadwick, 2012). Borehole sediment logging, displacement monitoring data and piezometric elevations measured in observation wells within the toe slope suggest the main body is failing along sub-horizontal, weak, basal shear surfaces within a highly plastic clay layer and overlying till diamicton (**Figure 2b**). Field observations indicate that earth materials in the main body are developing secondary tensional cracks and fissures above this slide surface. The depth of the sub-horizontal sliding surface is coincident with the bottom or slightly below the riverbed, so that continued down cutting of the river may result in further instability (Macciotta et al., 2014; Hendry et al., 2015; Schafer et al., 2015).

GPS and InSAR measurements indicate that the landslide experiences small increments of movement over time (cumulatively around 5 cm/yr), with peak movement from autumn to winter as river and groundwater reach minimum levels (Bunce and Chadwick, 2012; Macciotta et al., 2014; Hendry et al., 2015; Schafer et al., 2015). Peak river flows, bank erosion, bed scour, and highest differential between river and groundwater levels occur from spring to summer (cf. Eshraghian et al., 2008; Bunce and Chadwick, 2012). When the river is at its highest level, the slope displacement rate is at its lowest. This corresponds to an increased stability of the landslide due to a combination of a buttressing effect of the river and the increase in mobilized shear strength with increasing effective stress along the sliding surface (Bobrowsky et al., 2014; Macciotta et al., 2014; Hendry et al., 2015; Schafer et al., 2015).

Displacement sensors detected a general progressive increase in displacement following equipment installation in May 2013 (2.5 mm horizontal displacement and 2 mm of vertical displacement). Displacement rates increased between November 2014 and February 2015, corresponding to movement recorded by other monitoring systems. BOTDR monitoring curves for May, June and July 2013 showed a relative shift compared to the initial curve following installation in May 2013. Before going offline following a bear attack, four places with obvious strain were recognized at 1060 m, 1230 m, 1320 m and 1610 m that enclose the area of maximum displacement captured by GPS3 and likely represent hinge lines developing in the sagging retaining wall (Huntley et al., 2014).

1.4 Ripley Landslide: Knowledge Gaps in Landslide Composition and Geophysical Survey Objectives

GPS, borehole instrumentation, remote sensing and satellite interferometric techniques reveal limited information on the range of earth materials, landforms and subsurface nature of the Ripley Landslide. To expand the knowledge of the landslide, a field-based program combining surficial geology mapping with an array of geophysical techniques was undertaken between 2013 and 2015 (cf. Bichler et al., 2004; Best et al., 2009). The objective of the geophysical surveys was to

measure contrasts in the geophysical properties of unconsolidated sediments and bedrock, interpreted in the context of the known lithological units on site. Prior knowledge of geomechanical behaviours within and along unit boundaries (at other local landslides) allowed for an inference of the slide surface.

2. Terrestrial and Waterborne Geophysical Survey Methods

Field investigations were completed in the spring, summer and autumn of 2013, summer and fall of 2014, and winter and spring of 2015 using a variety of terrestrial and waterborne geophysical methods (**Table 1**). Survey objectives were to help: a) determine the thickness and types of subsurface materials; b) establish subsurface bulk conductivities; and c) infer the failure mechanisms of the landslide in the context of known geotechnical and geomechanical site conditions.

Geophysical cross-section lines were spaced across the breadth of the landslide and Thompson River to ensure reasonable diversity in coverage and to obtain a good estimate of the subsurface variability (**Figure 3**). Terrestrial cross-sections running approximately east-west extended beyond (east of) the head scarp of the landslide westward to the visible toe of the failure as defined by the river water level at the time of fieldwork (November 2013). Terrestrial cross-sections trending northeast to southwest were located between and parallel the CN and CPR rail tracks, and 10 m (east) of the CPR tracks, and extended beyond the lateral limits of the landslide. Traverses over water trended northeast to southwest to parallel the shoreline at the time of fieldwork (October-November 2014). Waterborne surveys were undertaken using 5 m and 6 m metal hulled jet boats, and a non-metallic 3 m white-water raft that contained the geophysics equipment.

All positional data were referenced to the 1983 Universal Transverse Mercator (UTM) Zone 10 North American coordinate system. Terrestrial geophysical data points were positioned by two Topcon Hiper Real Time Kinematics (RTK) Global Positioning System (GPS) units, with each unit simultaneously tracking up to 20 GPS and GLONASS (Globalnaya Navigazionnaya Sputnikovaya Sistema, or Global Navigation Satellite System) satellites under optimal conditions. At least 10 satellites were visible and typically between 14 and 17 satellites were accessible. A base station reference near GPS-4 was located with an accuracy within 4 cm horizontally and 4.5 cm vertically and used for all surveys. Real-time RTK corrections were broadcast to the second rover Topcon unit using a Positioning Data Link (PDL) radio modem. GPS locations were recorded continuously and at each stationary receiver location. The GPS positioning data were reviewed, corrected for antenna laybacks, heights and edited for erroneous data points during the data processing (Parry et al., 2014). Positional control for the waterborne surveys was provided using a Trimble GeoExplorer 6000 series hand-help GPS unit, the GPS/GLONASS receiver in a Garmin EchoMAP 50s and the Garmin Sounder 188 GPS (Bauman et al., 2015).

Geophysical technique	Date of fieldwork and desktop analysis	Lines as shown in Figure 3
Terrestrial Geophysics Campaign		
Terrestrial Electrical Resistivity Tomography (T-ERT)	November 2013	A – E (solid red)
Terrestrial Fixed Frequency Electromagnetic Induction (T-FEM)	November 2013	A – E (solid red)
Terrestrial Ground Penetrating Radar (GPR)	November 2013	A – F (solid red)
Terrestrial Seismic Refraction (SR)	November 2013	A – E (solid red)
Multi-spectral Surface Wave Analysis of SR data (MASW)	March 2015	A – E (solid red)
Waterborne Geophysics Campaign		
Acoustic Bathymetry (AB)	October 2014	1 – 10 (solid yellow)
Waterborne Electrical Resistivity Tomography (T-ERT)	October 2014	2 – 5 (dashed red)
Waterborne Electromagnetic Induction (W-EM)	November 2014	1 – 10 (solid yellow)
Waterborne Ground Penetrating Radar (GPR)	November 2014	1 – 10 (solid yellow)
Borehole Geophysics Campaign		
Borehole Gamma radiation (GR)	March 2015	
Borehole Induction Conductivity (IC)	March 2015	
Borehole Magnetic Susceptibility (MS)	March 2015	

Table 1 Geophysical techniques applied to the Ripley Landslide from 2013-2015 (after Parry et al., 2014; Bauman et al., 2015; Gugins and Candy 2015).

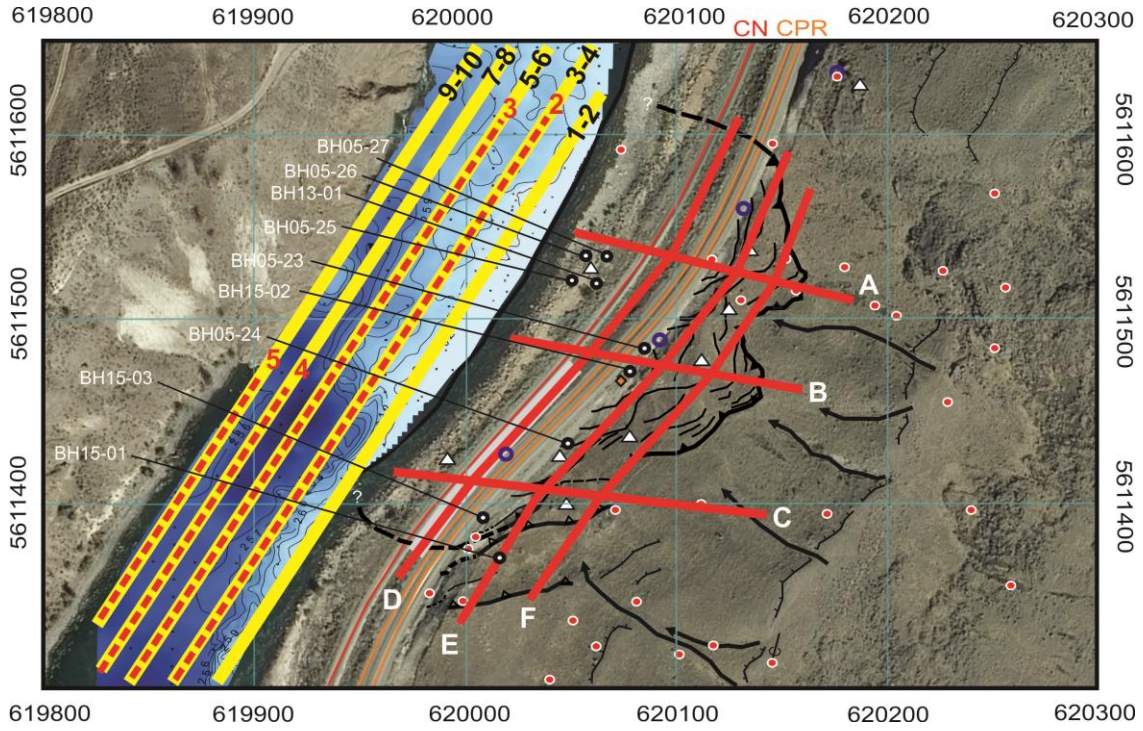

Figure 3 Geophysical cross-sections: A-F terrestrial survey lines (solid red); 2-5 waterborne ERT survey lines (dashed red); 1-10 waterborne AB, EM31, GPR survey lines (solid yellow) (after Parry et al., 2014; Bauman et al., 2015); locations of boreholes drilled for CN and CPR (BH05-23 to BH05-27, BH13-01, and BH15-01 to BH15-02) shown in relation to transect lines; borehole geophysical surveys completed for BH15-01, BH15-02 and BH15-03 (Candy et al., 2015); see Figure 2 for landform legend.

2.1 Terrestrial Geophysics Campaign

2.1.1 Terrestrial Electrical Resistivity Tomography (T-ERT)

The terrestrial ERT survey was conducted in November 2013. Five terrestrial ERT cross-section lines were surveyed. Three lines, 50 m apart, ran approximately E-W (**Figure 3**, lines A-C) and the remaining two, 10 m apart, ran approximately NE-SW (**Figure 3**, lines D, E). The E-W lines were positioned to extend beyond the headscarp to the east and as far west as the level of the river would allow. The NE-SW lines also were orientated to extend beyond the visible landslide limits to the north and south. One line was positioned above the fence east of the CPR tracks and a second between the CPR and CN rails farther west. With the exception of the morning of November 17th 2013 when there was a light dusting of snow, over the three days that the terrestrial ERT data were collected, there was no surface moisture on the ground to impact the data. Electrodes placed on the active floodplain of Thompson River in the west were placed in more saturated earth materials than the electrodes up-slope to the east. Areas east of the fence showed obvious signs of ground movement in the form of tension cracks and minor colluvial debris on the surface.

Variations in electrical resistivity of the subsurface were measured by applying direct current across a Wenner array of 48 ground electrodes spaced every 5 m along a 235 m cable. Electrodes were spaced approximately evenly across the site to ensure reasonable coverage of the survey area. Data were recorded using an IRIS Instruments Syscal R1 Plus and Switch Pro Box 96 72-channel system (**Figure 4a**). No area of the landslide had conditions that prevented electrodes from being placed in the ground. As a result, the ERT survey in this study had the most extensive and complete data coverage out of all the methods (see below). An initial resistivity check indicated the electrodes had relatively good contact with the ground (less than 1 kΩ), with the exception of a few locations on the upper slopes (between 5 and 10 kΩ) where scree was present on the surface. To ensure unbroken data coverage across the railroad tracks, the ERT cables were threaded under the rails so that trains could still travel freely without damaging equipment (Parry et al., 2014).

Resistivity values measured were bulk measurements of resistivity of various overlapping half spaces encompassed by the geometry of the four electrodes used in each measurement. These values were not specific to a particular layer or material and so represented ‘apparent resistivity’ measurements. The apparent resistivity pseudo-sections (apparent resistivity versus apparent depth) were processed using RES2DINV (Geotomo, 2012) to create 2D resistivity models of the subsurface. A forward modelling subroutine was used to calculate the apparent resistivity values for a given model. A non-linear least-squares optimization technique and inversion routine were used to compare the calculated apparent resistivity values and measured values. Based on this comparison the model was then iteratively modified to minimize the difference (Parry et al., 2015).

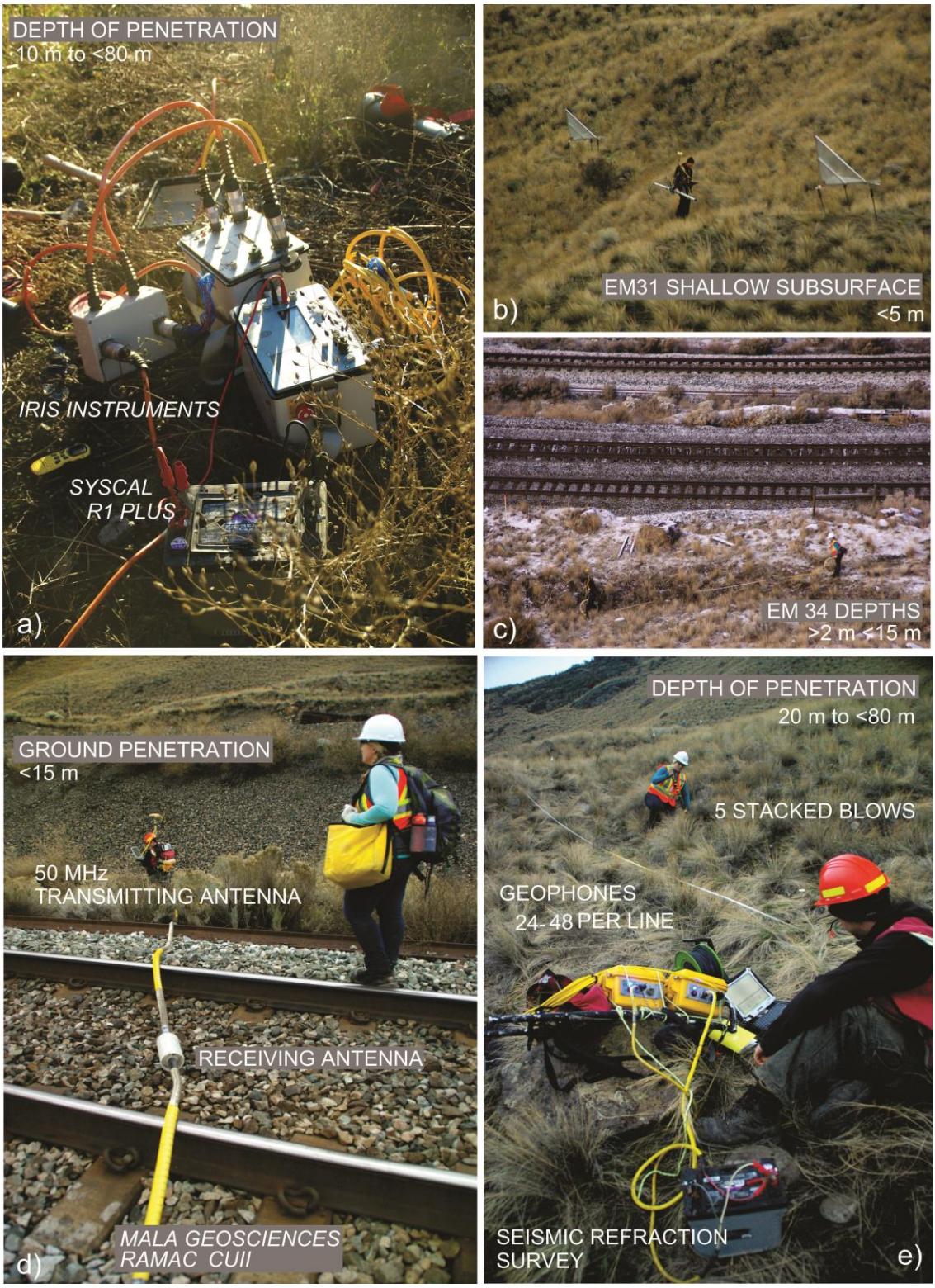

Figure 4 Terrestrial geophysical survey techniques applied to the Ripley Landslide, November 2013: a) T-ERT; b) EM31 T-FEM; c) EM34 T-FEM; d) 50 MHz GPR; e) Seismic Refraction (Parry et al., 2014).

2.1.2 Terrestrial Fixed Frequency-Domain Electromagnetic Induction (T-FEM)

Four terrestrial FEM cross-sections were surveyed. Three survey lines ran approximately E-W and the remainder ran approximately NW-SW east of the CPR tracks and upslope of the fence. The E-W lines were positioned to extend beyond the headscarp (**Figure 3**, lines A-C). The NE-SW line was also oriented to extend beyond the visible landslide limits in the north and south (**Figure 3**, Line E). Geonics EM-31 and EM-34 systems operating in the horizontal co-planar (vertical dipole) mode were used to continuously acquire electromagnetic terrain conductivity (mS/m) data (cf. Best et al., 2009). These datasets were integrated with real-time global positioning information along each transect line.

EM31 survey data were collected in continuous acquisition mode by walking each survey profile in turn (**Figure 4b**). The Geonics Ltd. EM31 Terrain Conductivity Meter boom containing the transmitter and receiver coils was maintained approximately horizontal on all lines, although in areas with steeper grades this required rotating the boom so it was parallel to the cross slope. As a result, the orientation of the boom with respect to the lines varied but was not an issue in the data analysis. Buried linear conductive features were not encountered up-slope of the fence and rail tracks. EM31 data were edited to remove erroneous data values, matched to the GPS information, and then processed in two modes. First, apparent conductivities were plotted and contoured using the Golden Surfer Version10 mapping program. EM31 data was irregularly spaced, so trends in the data were best expressed using the kriging geostatistical gridding method. Data were interpolated between measurement points where paths were farther apart than 2.5 m EM31 measurement swath. Second, the data were input into the EMIGMA Version 8.6 electromagnetic modelling program to combine this information with EM34 data and generate an inverted conductivity cross-section along each survey profile line (Parry et al., 2014).

For this survey, a Geonics Ltd. EM34 system with 10 m and 20 m intercoil spacing was used in vertical and horizontal modes (**Figure 4c**). Data were recorded at stationary points every 10 m along each survey profile. By convention, the measurement point was taken to be the mid-point between the receiver coil and the transmitter coil. Nulling the instrument to obtain accurate conductivity values proved difficult at some locations because of differences in height between the transmitter and receiver coils. Real-time differential GPS locations were recorded at each receiver station with the receiver coil leading the transmitter coil on all survey profiles. Once collected and organized, EM31 and EM34 data were interpolated and inverted, using EMIGMA Version 8.6 electromagnetic modelling software (Parry et al., 2014).

2.1.3 Terrestrial Ground Penetrating Radar (T-GPR)

The terrestrial GPR survey was conducted in November 2013. Terrestrial GPR data were collected along six different profile lines for this survey spaced approximately evenly across the site to ensure reasonable coverage. Coverage was interrupted where the cross-section lines cross the rail tracks since the metal interferes with the radar signal. Three lines, 50 m apart, run approximately E-W (**Figure 3**, lines A-C); and the remaining three run 10 m apart, approximately NE-SW (**Figure 3**, lines D-F). The E-W lines were positioned to extend beyond the headscarp in the east and as far west as the start of the Thompson River floodplain. The NE-SW oriented lines also were orientated to extend beyond the visual limits of the slide to the north and the east. Two

lines were positioned above the fence east of the CPR tracks (T-GPR lines E and F) and the third was positioned between the CPR and CN tracks farther west (T-GPR Line D).

A Mala Geosciences Ramac CUII with both 100 MHz and 50 MHz RTA antennas was used for the T-GPR survey (**Figure 4d**). This impulse GPR system was used to direct a short duration broadband EM pulse into the ground from a transmitter source (Parry et al., 2014). The electromagnetic pulse was reflected back to the surface at various increasing time intervals due to changes in the dielectric properties of the subsurface. Following an evaluation of preliminary test profiles on site, the 50 MHz antennas were selected to identify potential stratigraphic layers that might indicate the presence of perched groundwater or clay layers. To meet this objective, the loss in vertical resolution of thin layers and near surface detail was considered acceptable to maximize depth penetration. Data collection window lengths were sufficient to collect up to 20 m depth. The transmitter-receiver separation was fixed at 1 m and the two antennae were dragged over the slope (**Figure 4d**). Data was continuously collected and georeferenced with GPS measurements. The measurement point was located at the midpoint between the transmitter and receiver antennae. T-GPR data files were plotted as sections representing two way travel time (vertical axis) versus position of the transmitter-receiver midpoint (**Figure 4d**). Depth in metres was also plotted on a vertical axis using the velocity of 0.1 m/ns (i.e., an average dielectric constant of 9). Processing of T-GPR data was limited to trace averaging and filtering (cf. Best et al. 2009).

Terrestrial GPR data were recorded using a Panasonic Toughbook laptop with soundings recorded in 'free run' mode at a rate of approximately 15 soundings per second, and data collected at a walking speed (slower while going upslope). T-GPR data coverage was limited to areas far enough away from the railroad tracks to avoid 'ringing' in the data from the steel rail tracks. As a result, lines were collected in areas east of the upslope fence and beneath the CN railroad tracks in the west. Data were collected between the CPR and CN tracks, but due to the proximity to both rail lines, the data are of poorer quality. Building on conventional methodologies (cf. Morey, 1974; Ulruksen, 1982; Noon et al., 1994), T-GPR data were processed using a proprietary processing package developed by Tetratech EBA using Matlab (Mathworks). Basic processing steps applied to the data included low frequency filtering (dewow), drift corrections, logarithmic gain and topographic corrections. A common mid-point velocity analysis was not attempted because of the high sub-surface relief: a flat, parallel reflector to the ground surface is ideally required (Parry et al., 2014).

2.1.4 Terrestrial Seismic Refraction Survey (SR)

The seismic refraction (SR) survey was conducted in November 2013. Five SR lines were spaced evenly across the site to ensure reasonable coverage of the landslide: three, 50 m apart, ran approximately E-W (**Figure 3**, lines A-C); and two, 10 m apart, ran NE-SW (**Figure 3**, lines D-E). The E-W lines were positioned to extend beyond the head scarp in the east and ran as far west as the Thompson River floodplain. The NE-SW cross-section lines also were oriented to extend beyond the north and south limits of the landslide. Seismic refraction Line D was positioned between the CPR and CN; SR Line E was positioned above the fence east of the CPR tracks.

Acoustic energy was provide by multiple blows from a 5 kg sledgehammer delivered to 1 cm thick steel plate placed in contact with the sloping ground surface: an early attempt to use a Betsy gun was abandoned for safety concerns (**Figure 4e**). The loose surface material at the site also posed a problem for the sledgehammer and plate, making it difficult to get enough energy into the ground for adequate seismic records. This was counteracted by stacking the data with 3 to 5 shots per location to improve data signal-to-noise levels. Depth of penetration using stacked sledgehammer blows was greater than 10 m.

Data were recorded using a Panasonic Toughbook with Seismodule Controller Seismic recording software, two Geometrics Geodes and 24-48 geophones at 5 m spacing (**Figure 4e**). Refraction data were later processed and modelled using the ray tracing method in ReflexW Version 7.2 (Sandmeier, 2012). Results were back-checked with reasonable agreement for SR Line A using Rayfract Version 3.1.7. Seismic data files were plotted as sections representing two way travel time on the vertical axis versus position of geophones on the horizontal axis (cf. Yilmaz, 2001).

2.1.5 Terrestrial Multi-Spectral Analysis of Surface Waves (MASW)

Multi-spectral processing of surface waves was carried out on all five seismic refraction traverses. A total of 700 m of MASW processing were completed on the SR data to determine overburden and bedrock shear wave velocities (Gugins and Candy 2015). Data were collected over the full seismic spread and results plotted as vertical profiles. Limitations to processing and interpreting the data included the reflection and scattering of surface and body waves due to the extreme surface topography, subsurface concentrations of boulders and isolated sediment lenses with contrasting seismic properties (Gugins and Candy, 2015).

2.2 Waterborne Geophysics Campaign

2.2.1 Acoustic Bathymetry (AB)

Acoustic bathymetry data were collected using a Garmin EchoMAP 50s and a 77/200 kHz sonar transducer. The transducer was secured to the jet boat approximately 0.4 m below the water surface (mbws). Each bathymetric measurement was paired with a GPS location from the built-in GPS/GLONASS receiver. Data were collected continuously while travelling on upstream and downstream survey passes in the 5 m jet boat.

Figure 5 Waterborne geophysics applied over the Thompson River, October-November 2014: a) AB and W-ERT set-up, including jet boat, ERT streamer and depth sounder; b) W-ERT data collection in the jet boat; c) W-EM31 set-up operating mid-channel in Thompson River; d) W-GPR set-up operating along the right channel bank (Bauman et al., 2015).

2.2.2 Waterborne Electrical Resistivity Tomography (W-ERT)

The waterborne ERT survey was conducted in October 2014. Four W-ERT cross-sections were surveyed, running approximately parallel to NE-SW terrestrial lines (**Figure 3**). A reverse Wenner array was used with a minimum electrode separation of 10 m to allow imaging to a maximum depth of investigation 27 m to 32 m below water surface (mbws) (Bauman et al., 2015). The W-ERT system used a 10-channel IRIS Instruments Syscal Pro resistivity transmitter/receiver with a thirteen takeout towed-streamer run from the stern of the 5 m jet boat (**Figure 5a**). The ERT instrument, capable of injecting up to 2.5 amperes to provide high quality data, recorded in a near continuous fashion with voltage measured across each of its 10 channels.

Measurements were displayed and stored in real-time on a Panasonic Toughbook connected to the instrument (**Figure 5b**). The laptop remotely controlled the instrument with the software package SYSMAR. Each measurement was recorded with a GPS position and water depth measurement collected by the Garmin Sounder 188 GPS. Consecutive measurements were triggered by a pre-set spacing and at 2 second intervals (minimum) to accommodate the update rate for out-going GPS information (Bauman et al., 2015).

2.2.3 Waterborne Electromagnetic Induction Methodology (W-EM31)

The waterborne frequency domain EM survey was conducted in November 2014. Terrain conductivity measurements beneath the Thompson River were taken using a Geonics Ltd. EM31 system onboard a white-water raft (**Figure 5c**). This (metal-free) vessel was towed upstream by the 6m jet boat, detached at the northern survey boundary, and then guided down to the southern survey boundary while measurements were collected (**Figure 3**). The W-EM3 terrain conductivity data (mS/m) were collected in a vertical dipole mode coil orientation approximately 50 cm above the water surface. Georeferenced data points were collected approximately every metre along traverse lines 1 to 7 m apart (Bauman et al., 2015).

2.2.4 Waterborne Ground Penetrating Radar (W-GPR)

The W-GPR survey was conducted in November 2014, with data collected along ten survey lines (W-GPR lines 1 through 10) while travelling downstream in the white water raft (**Figure 3**; **Figure 5d**). Georeferenced waterborne GPR data were collected using a GroundRadar UltraGPR 10 to 80 MHz instrument with a nominal source frequency of 30 MHz (Bauman et al., 2015). The instrument was operated in 'free-run' mode using a stacking interval of 32,000/second, while simultaneously pairing radar traces with GPS data. For this survey, the transmitter and receiver antennae were contained inside ABS pipe pontoons and secured to opposite outboard sides of the raft (**Figure 5d**). This avoided loss of Bluetooth connectivity and allowed more control over the location of the transmitting and receiving antennae (Bauman et al., 2015). The W-GPR processing by International GroundRadar Consulting Inc. included geo-referencing, elevation correction, dewow filtering, amplitude gain, bandpass frequency filtering, and time-to-depth corrections using velocities determined by analyzing the shape of diffraction hyperbolae from subsurface objects. W-GPR data files were plotted as sections representing two way travel time (vertical axis) versus position of the transmitter-receiver midpoint. Depth in metres was also plotted on a vertical axis using a radar velocity of 0.06 m/ns; i.e., an average dielectric constant of 25 (Bauman et al. 2015). In addition, a river bottom elevation map was produced from the GPR data for comparison with the acoustic bathymetry results (**Figure 6b**).

2.3 Borehole Geophysics Campaign

2.3.1 Borehole Geophysical Survey (GR, EM and MS)

Three 17 m deep boreholes located directly adjacent to the CPR tracks were drilled in February and March 2015 (**Figure 2**, **Figure 6a**). Borehole geophysical surveying, conducted in March 2015, involved the vertical logging of variations in natural gamma radiation (GR) measured in counts per second (cps), electromagnetic induction (EM) measured in milliSiemens per metre (mS m^{-1}), and magnetic susceptibility (MS) calibrated in parts per thousand (ppt).

Figure 6 a) Location of boreholes drilled and logged in February-March 2015; b) Borehole logging set-up measuring natural gamma, conductivity and magnetic susceptibility (Gugins and Candy, 2015).

Down-hole surveys were carried out using a Mount Sopris MGX II digital borehole logging system controlled by a Notebook laptop computer. A portable gasoline generator provided isolated 115 Volt AC power for the instruments. The system used Poly Probe technology that allowed the acquisition of multiple logs simultaneously on a single conductor pair. A motorized 4MXB-1000 winch with a 0.125" diameter steel armoured single-conductor cable was used for borehole logging. Equipment was set up adjacent to the borehole to be logged and calibrated to establish the datum at the casing top (**Figure 5b**). All boreholes were logged top to bottom, and bottom to top. Logging was carried out at a speed of 2 metres per minute or less. This multiple pass procedure was adopted to ensure high resolution and repeatability of data. Records were monitored in real time for quality assurance during the logging operation (Gugins and Candy, 2015). The natural gamma, induction conductivity and magnetic susceptibility log data were recorded with Mt. Sopris MS LOG software. Borehole geophysical logs were presented using the Surfer (Golden Software) program (Gugins and Candy, 2015).

Downhole natural gamma response (GR) measurements were collected with a 2PGA-1000 Poly-Gamma probe. The probe measured natural gamma radiation (as cps) with a large sodium iodide scintillometer. Although the gamma probe was sensitive out to 20 cm, most of the counts came from the first 5 cm outside of the borehole casing.

Downhole induction conductivity (IC) was measured using a 2PIA-1000 poly-induction EMP-2493 probe. This EM probe provided measurements of the apparent electrical conductivity of unconsolidated deposits and bedrock surrounding the three boreholes using electromagnetic induction techniques (McNeill, 1986; Gugins and Candy, 2015). The EMP-2493 probe

transmitted an electromagnetic signal that passed through the plastic pipe wall of the borehole lining, penetrating to a depth of approximately 25 cm. The probe then measured the strength of the returned response to the signal, with the conductivity response calibrated to provide a range of data from 0 to 100 mS m^{-1}. The unit employed coaxial coil geometry with an intercoil spacing of 50 cm to provide a substantial radius of exploration into the surrounding earth, while maintaining excellent vertical resolution.

Downhole magnetic susceptibility (MS) measurements were taken with a 2PIA-1000 poly-induction 2MSA-1000 magnetic susceptibility probe. Similar to the EM conductivity probe, the unit employed coaxial geometry with an intercoil spacing of 50 cm to provide a suitable exploration radius (25 cm) while maintaining vertical resolution. When the probe is operated in MS mode, the readings provided an indication of the relative variation of magnetically susceptible minerals (e.g., magnetite, pyrrhotite and ilmenite). Magnetic susceptibility was measured as a percent of primary magnetic field and calibrated in units of parts per thousand (ppt). The MS probe was not influenced by the strength of the earth's magnetic field or variations in remnant magnetism of the encompassing glacial deposits and bedrock (Gugins and Candy, 2015).

3. Terrestrial Geophysics Results and Interpretation

Terrestrial geophysical surveys provide measurements of the variation of physical and chemical properties of the sub-surface, allowing for an interpretation of unit thickness, and depth to bedrock (**Table 2**). These variations, along with a priori knowledge of geotechnical conditions on site, allow for an interpretation of the internal structures of the slide providing insight into potential failure mechanisms.

3.1 Interpretation of Terrestrial Electrical Resistivity Tomography Results

The T-ERT inversion results are presented as colour-contoured 2D depth profiles for each survey line (**Figure 7**). Detailed resistivity images of the subsurface to depths greater than 10 m and less than 80 m were possible by the redundant sampling of electrode combinations (Parry et al., 2014). The direct current T-ERT system provided useful information on the internal properties of the landslide (**Figure 7**).

Resistive contrasts were seen between surficial units and underlying bedrock (**Table 2**). Small and irregular anomalies, areas of complex subsurface geometry and groundwater are resolved along all five cross-section lines (**Figure 7a**, T-ERT Lines A-E). Comparing field observations (Huntley and Bobrowsky, 2014; **Figure 2**) to the T-ERT profiles, non-porous, fractured bedrock (magnetite- and ilmenite-bearing andesite, rhyolite and pyroclastic rocks) and coarse, rapidly drained ballast (unit 10), colluvium (units 2 and 8), alluvial (unit 9), and unsaturated glaciofluvial sediments (unit 7) have higher apparent resistivity values (greater than 100 Ωm; orange to red on cross-sections). Moderately to well-drained till (unit 4), glaciofluvial outwash (unit 7) and colluviated bedrock (coarse-grained facies, unit 2) at depth are moderately resistive, with values greater than 50 Ωm to less than 100 Ωm (yellow to green on cross-sections). Areas with low resistivity values (below 50 Ωm; blue to violet on cross-sections) include poorly or imperfectly drained clay-silt deposits (fine-grained facies, units 2, 3 and 5), or landslide structures containing groundwater (Parry et al., 2014). Very shallow (< 5 m) sub-vertical features correspond to tension cracks observed across the main landslide body (**Figure 2a**). Shallow (< 20 m), sub-horizontal planar to curvilinear features observed on all cross-section lines are interpreted as lithological changes, unit boundaries and translational or rotational slide planes within units 2, 3, 4 and 5 (**Figure 7a**).

T-ERT Line A is the northernmost E-W cross-section (**Figure 7a**). A relatively resistive layer (>500 Ωm) is dominant along the bottom of the eastern portion of the profile. This electrical feature is likely representative of competent bedrock (unit 1) as evidenced by observed outcrops (Huntley and Bobrowsky, 2014; **Figure 2a**) and the recovery of andesite from BH05-25 to BH05-27 and BH13-01 (**Figure 2b**). It is possible that there is a layer of weathered and/or less competent bedrock on top of the bedrock layer causing the slightly lower resistance values layered on top (coarse facies of unit 2). Scree observed at the steepest point on the easternmost part of the line (unit 8) accounts for the higher resistance values close to the surface on the very eastern section of the line (Parry et al., 2014). A relatively conductive (25 Ωm to 125 Ωm) section is seen from surface to depth on the western half of the profile and then gradually becomes layered between two more resistive layers in the centre of the profile. This area most likely represents glaciolacustrine clay layers (units 3 and 5). The third feature is a shallow resistor (125

Ωm to 500 Ωm) that extends from surface to approximately 3 to 6 m depth. Based on resistance values and field observations, this is most likely till (unit 4). Tension cracks developed in till suggest that this shallow resistor is moving on a sub-horizontal translational slide plane within the underlying conductive (clay) layer. Additional sub-surface structure is evident with a contouring scale detailing resistivity values between 25 Ωm and 125 Ωm (**Figure 7b**).

T-ERT Line B is the central E-W cross-section (**Figure 7a**). A relatively resistive layer (>500 Ωm) along the bottom of the eastern portion of the profile represents competent andesitic and rhyolitic bedrock (unit 1) as evidenced by observed outcrops (Huntley and Bobrowsky, 2014; **Figure 2a**) and the recovery of massive andesite from BH05-24, BH15-02 and BH15-03 (**Figure 2b**; and see below, Section 5.1). Slightly lower resistance values above bedrock are interpreted to represent clast-supported diamicton and deformed clay, similar to deposits observed in outcrop overlying bedrock exposures (unit 2). A relatively conductive (25 Ωm to 125 Ωm) layer is present from surface to depth along the western half of the profile. It becomes sandwiched between two resistive layers in the centre to the eastern part of the profile. Based on resistance values, field observations and borehole information, this area is glaciolacustrine clay (units 3 and 5). A more detailed resistivity image of subsurface structures is apparent using a contouring scale between 25 Ωm and 125 Ωm (**Figure 7b**). Up slope of the train tracks, shallow, relatively moderate resistors (125 Ωm to 500 Ωm) extend from surface to approximately 4 m to 10 m depth. Field observations in this area (Huntley and Bobrowsky, 2014; **Figure 2**) and resistance values suggest the material is till diamicton (unit 4). Surface tension cracks in surface exposures of till are surface expressions of active translational or rotational movement along slide planes within the high conductivity layer below. Relatively lower resistivity values up-slope suggests either finer grained material (unit 5) or higher moisture levels in till diamicton, glaciolacustrine clay, glaciofluvial gravels (unit 6) and alluvial fan deposits (unit 7). The distribution of pore water fluids within this surficial layer at this location may indicate that moisture is feeding into the underlying glaciolacustrine clay and colluvium (units 2 and 3) and bedrock (unit 1). Resistive surficial material, starting on the eastern side of the CN rail tracks and ending in the Thompson River bed, consists of the alluvial boulder field exposed between the rail lines and the low water mark at the river's edge (unit 9) and coarse rail ballast (unit 10).

T-ERT Line C is the southernmost E-W cross-section (**Figure 7a**). A relatively resistive layer (>500 Ωm), dominant along the bottom of the eastern portion of the profile is likely bedrock (unit 1). This interpretation is supported by field observations of andesite outcrops in the vicinity of Line C (**Figure 2a**) and the recovery of massive andesite from BH05-23, BH15-01 and BH15-03 (**Figure 2b**; and see below, Section 5.1). However, unlike the other two E-W cross-sections, this line appears to have deeper competent bedrock and a more resistive layer lying above a less resistive till diamicton (unit 4), interpreted as an ice-rafted bedrock block. A conductive (25 Ωm to 125 Ωm) area is present from surface to depth in the centre of the profile. This area most likely consists of the glaciolacustrine clay and silt (units 2 and 3). Layering structures are evident when resistivity values between 25 Ωm and 125 Ωm are emphasized (**Figure 7b**). A shallow, relatively moderate resistor (125 Ωm to 500 Ωm) beneath the CN and CPR tracks extends from surface to approximately 2 to 10 m depth and appears to continue farther into the Thompson River bed. This covers the area between the rail tracks and the low water mark at the river's edge. The material

from surface observations likely consists of the alluvial boulder field (unit 9) and ballast (unit 10). Higher on the slope, resistivity values are between 125 Ωm and 500 Ωm and likely represent till (unit 4) overlying bedrock (unit 1). Thickness estimates range from 7m to 15 m. A pocket of less resistive material at the top of the profile line suggests either fine-grained sediment (unit 7) or increased soil moisture levels locally within sand and gravel-rich glaciofluvial outwash (unit 6).

T-ERT Line D is the westernmost NE-SW cross-section (**Figure 7a**). In the south, starting at approximately 20 m depth a relatively resistive layer (>500 Ωm) is most likely competent bedrock (unit 1) based on these resistance values, correlation with other ERT lines where bedrock outcrops were observed (Huntley and Bobrowsky, 2014), and with nearby boreholes (BH05-23, BH15-01 and BH15-03, see Section 5.1). Slighter lower resistance contours (125 Ωm to 500 Ωm) surround this section and could be less competent bedrock (unit1) or bouldery clay-rich colluvial diamicton (unit 2). A relatively conductive layer (125 Ωm to 500 Ωm) is present that extends from surface to the top of the deeper resistive layers in the southern half of the profile, and then gets deeper to the north where it extends past the bottom of the profile. Field observations and resistance values are consistent with glaciolacustrine clay and till diamicton layers (units 3 and 4). Layering is evident if a contouring scale between 25 Ωm and 125 Ωm is used (**Figure 7b**).

Four shallow moderate resistors (125 Ωm to 500 Ωm) are recorded on this line. In the south, there is a high resistance anomaly that could be a product of the inversion process, but may be real since it is also visible in raw data. Electrodes were moved multiple times during T-ERT data collection in an attempt to get lower contact resistance with no success at this location. Different moisture levels were not observed at surface, nor were there any other obvious reason to explain poor resistive contact. Electrodes were difficult to insert and remove in this area, with subsurface material being sticky, hard and plastic (Parry et al., 2014). Poor coupling with geophones and low seismic velocity was also observed in this area. A second shallow resistor is approximately 1 m deep at the intersection with Line C where a shallow resistor with similar properties is also recorded. The third resistor ranges from 1 m to 6 m depth at the intersection between Line B and Line D. The final shallow anomaly on the northern part of this line is approximately 5 m deep. This resistive layer is similar to those on lines A, B and C and represents coarse ballast between the rail lines (unit 10) and coarse fluvial sediments exposed on the Thompson River flood plain (unit 9).

T-ERT Line E is the easternmost NE-SW cross-section (**Figure 7a**). At the southern end, a strong resistive layer (>500 Ωm) observed at approximately 20 m depth, is most likely competent bedrock (unit 1) based on the range of resistance values and correlation with other ERT lines where bedrock outcrops were observed and recorded in boreholes (BH15-01 and BH15-03, Section 5.1). Slightly lower resistance contours (125 Ωm to 500 Ωm) surround this section. A similar area of resistance recorded in the central section could be less competent bedrock (unit 1) or colluvial diamicton and clay (units 2 and 3). A moderately strong conductor (125 Ωm to 500 Ωm) is present along the entire extent of the profile at varying depths. This layer extends from surface to the top of bedrock layers in the southern half of the profile; extends to depth in the centre of the profile; and becomes shallower in the northern part of the profile where it is sandwiched between relatively resistive glaciolacustrine clay (unit 3) and till diamicton (unit 4).

Applying a contour scale detailing resistivity values between 25 Ωm and 125 Ωm reveals further structure (**Figure 7b**).

Surficial geology unit	**Earth material** Description; structure; drainage	**T-ERT** Ωm	**W-ERT** Ωm	**T-FEM** Modelled conductivity mS m^{-1} *Resistivity Ωm*	**W-EM** Modelled conductivity mS m^{-1} Bathymetry corrected *Resistivity Ωm*	**T-GPR, W-GPR** Origin, character, strength of reflectors	**Seismic Refraction** P-wave velocity m s^{-1}	**Shear wave** Velocity m s^{-1}
Unit 10 */*** Anthro-pogenic	Cobble and boulder ballast; rapidly-drained	<500	-	<5 *>200*	-	Boulders P, S Unit contact L, W	250 - 600	240 - 280
Unit 9 */*** Alluvial *May contain ground-water seeps*	Boulders and sand; rapidly drained; saturated	<500	100 - 450	<5 *>200*	30 – 60 *33 - 17*	Boulders P, S Unit contact L, W	600 - 3500	240 - 280
Unit 8 */*** Colluvial	Blocks, gravel, sand, clast-supported diamicton; rapidly-drained	<500	-	<20 *>50*	-	Boulders P, M - S Unit contact L, W	250 - 600	100 - 240
Unit 7 */*** Alluvial	Sand, silt and minor gravel; well-drained	125 - 500	-	<20 *>50*	-	Basal contact L, W	250 - 600	100 - 200
Unit 6 *** Glaciofluvial	Gravel and sand; rapidly-drained	125 - 500	-	<20 *>50*	-	Boulders P, M Basal contact L, W	250	100 - 280
Unit 5 */** Glacio-lacustrine	Silt and clay; deformed; poorly-drained	<125	-	>20 *<50*	-	Groundwater L, W - M Basal contact L, W - M	1400 – 2300	240 - 300
Unit 4 **/*** Till	Silt-clay matrix-supported diamicton; moderately-drained	125 - 500	25 - 150	>20 *<50*	15 – 30 *67 - 33*	Boulders P, M Groundwater L, W - M Basal contact L, W - M	400 - 600	280 - 380
Unit 3 */** Glacio-lacustrine	Clay and silt; deformed; poorly-drained, stiff to hard	<125	25 – 100	>20 *<50*	15 – 30 *67 - 33*	Groundwater L, W - M Basal contact L, M - S	1400 – 2300	300 - 500
Unit 2 */** Colluvial	Clay, poorly-drained, stiff to hard; and blocks, gravel, sand, clast-supported diamicton; well-drained	<500	150 – 500	<20 *>50*	15 – 30 *67 - 33*	Basal contact L, M - S	600 - 3500	380 - 500
Unit 1 **/*** Bedrock *May contain ground-water*	Andesite, rhyolite and pyroclastic beds; weathered, fractured; well-drained	>500	1,000 - >3,000	<5 *>200*	<15 *>67*	No internal reflectors	3500 - 4000 (weathered) >4000 (pristine)	500 - 700

Table 2 Summary of modelled terrestrial and waterborne ERT, FEM, GPR and Seismic properties of surficial units and bedrock at the Ripley Landslide; * may contain groundwater seeps / ** may contain groundwater in fractures, partings and porous beds / *** may contain downward percolating surface waters; GPR reflectors, P – point, L – linear, S-strong, M – moderate, W – weak.

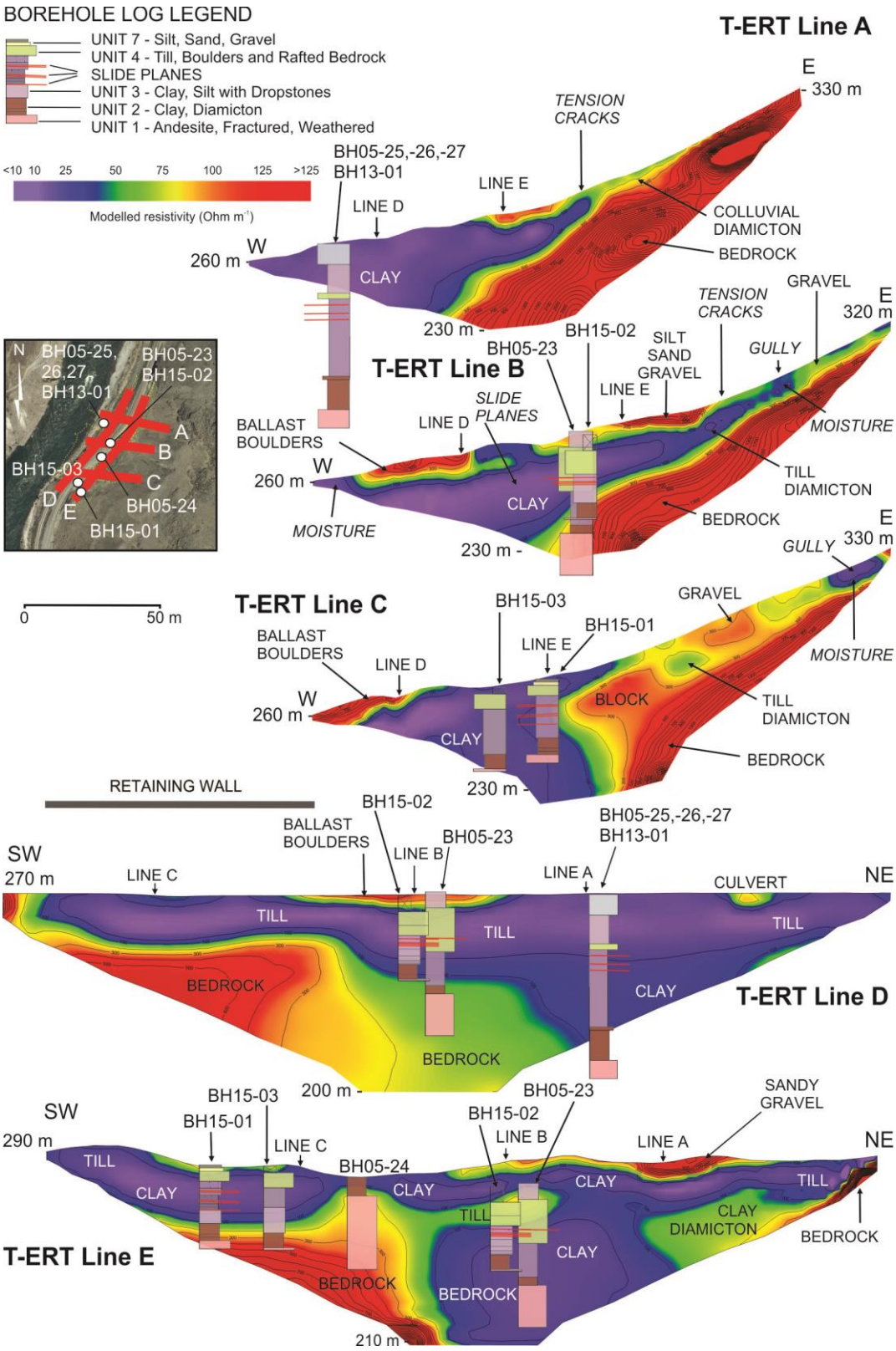

Figure 7a 2D resistivity models of the subsurface along T-ERT lines A-E; resistivity range <10 Ωm to >125 Ωm (after Parry et al., 2014); key features and lithologies are interpreted from field observations and graphic logs of boreholes BH15-01, BH15-02 and BH15-03 superimposed on profiles.

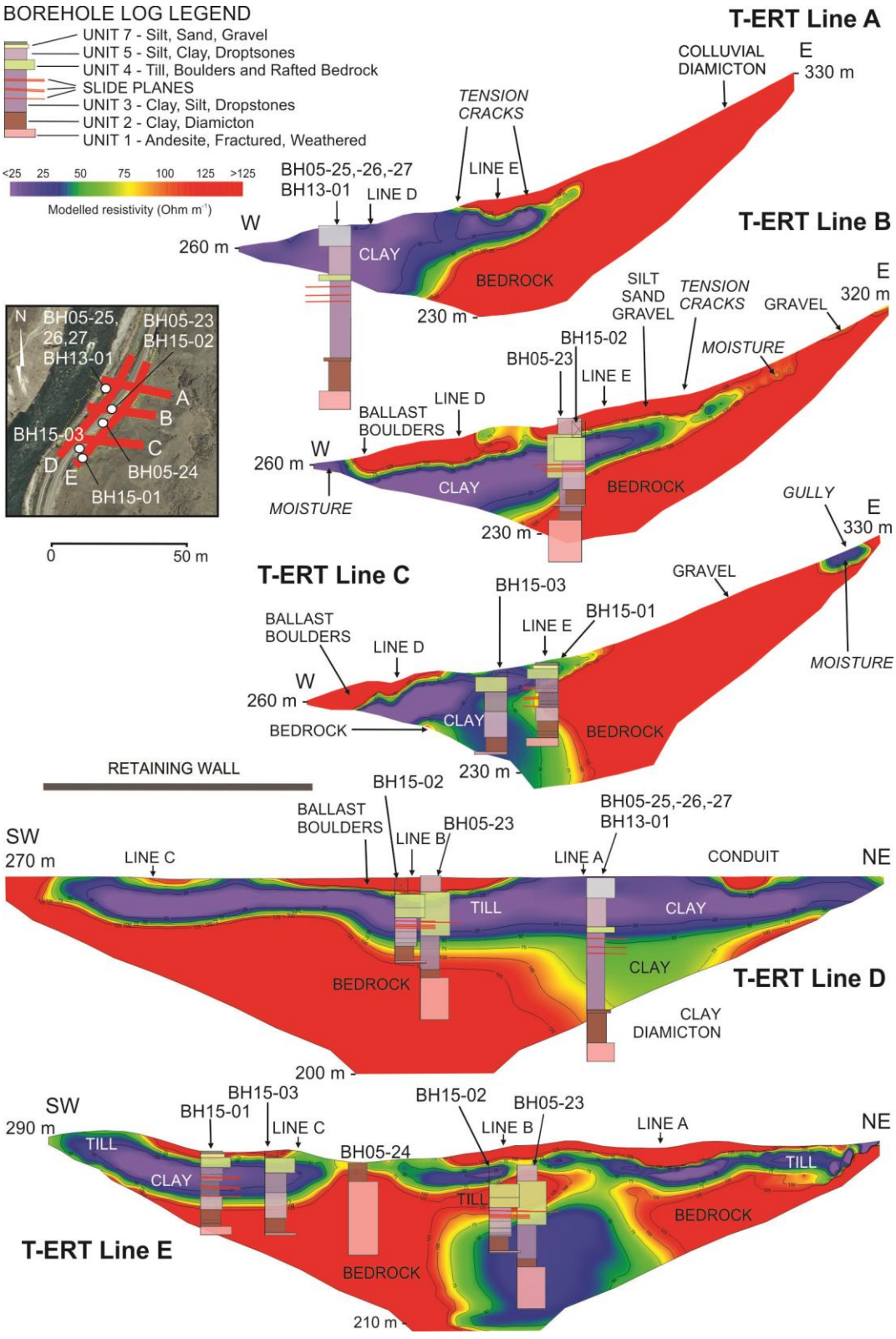

Figure 7b 2D resistivity models of the subsurface along T-ERT lines A-E; resistivity range <25 Ωm to >125 Ωm (after Parry et al., 2014); key features and lithologies are interpreted from field observations and graphic logs of boreholes BH15-01, BH15-02 and BH15-03 superimposed on profiles.

Two shallow resistors (125 Ωm to 500 Ωm) have been recorded on this line. The first in the south ranges from 1 m to 3 m depth. The second is more central and ranges in depth from 1 m to 10 m. The intersection between lines B and E occurs over this area. Since these resistors correlate to similar resistive points in lines A, B, C and D it is likely they consist of till (unit 4) and colluvial gravels (unit 8). Tension cracks observed in this second area are surface manifestations of movement of coherent blocks of till and colluvium moving translationally along sub-surface slide planes. The geophysical profiles suggest these failure surfaces are developed in underlying till (unit 4) and glaciolacustrine clay (units 2 and 3).

3.2 Interpretation of Terrestrial Electromagnetic Induction Results

Ground penetration depths ranged from less than 5 m for EM-31, to greater than 2 m and less than 15 m with EM-34. Porosity, relative pore saturation, total dissolved solids, soil content and temperature all affect the conductivity of subsurface earth materials. Clay and silt are typically more conductive than sand and gravel. Surface and subsurface metal, including fences, steel-frame structures, rail tracks, freight cars, train engines and vehicles can produce negative or high values due to the non-linear response of the instrument and violation of the low induction response required for the calibration to directly measure electromagnetic conductivity (McNeill, 1980a; 1980b). Terrain conductivity data are reported in units of milliSiemens per metre (mS m^{-1}, **Table 2**).

EM34data were recorded along four different profile lines. Data were not collected along Line D because the presence of the steel rails influenced the reading and biased the results. EM34 data were combined with the EM31 data and the modelled results are presented as conductivity cross-sections in **Figure 8**. By combining profiles from EM-31 and EM-34 techniques, a detailed image of the near-surface and deep-seated earth materials was generated (cf. Best et al. 2009). Increasing ground conductivity is indicated by a change from low values (blue and violet) to moderate (green and yellow) to high values (orange and red). The overall ranges of conductivities recorded with the inverted model on this site are relatively low, especially in the upper slope areas indicating predominantly resistive materials over the depth of measurement for the T-FEM system (Parry et al., 2014). These values are in close agreement to the borehole conductivities recorded in BH15-01, BH15-02 and BH15-03 (see below, Section 5.1).

Resistive bedrock and surficial deposits in steep terrain is a difficult environment for FEM methodologies (Best et al., 2009). Limited information on the thickness and lithology of surficial earth materials, bedrock and landslide structure on land was provided by the terrestrial EM-31 survey. Minor variations in the conductivity readings do not correlate well with geological structures. Subtle variations in EM-34 conductivity correlate with lows in the ERT data. Strong conductive contrasts were seen between the surficial units and underlying bedrock (**Figure 8**). Colluvial diamictons (units 2 and 8), till (unit 4) and coarser granular deposits (units 6 and 9) typically have conductivity values lower 25 mS m^{-1} (yellow and green on cross-sections). Glaciolacustrine clays (units 3 and 5) have conductivity values greater than 20 mS m^{-1} (red on cross-sections). Bedrock conductivities are below 5 mS m^{-1} (violet and blue on cross-sections).

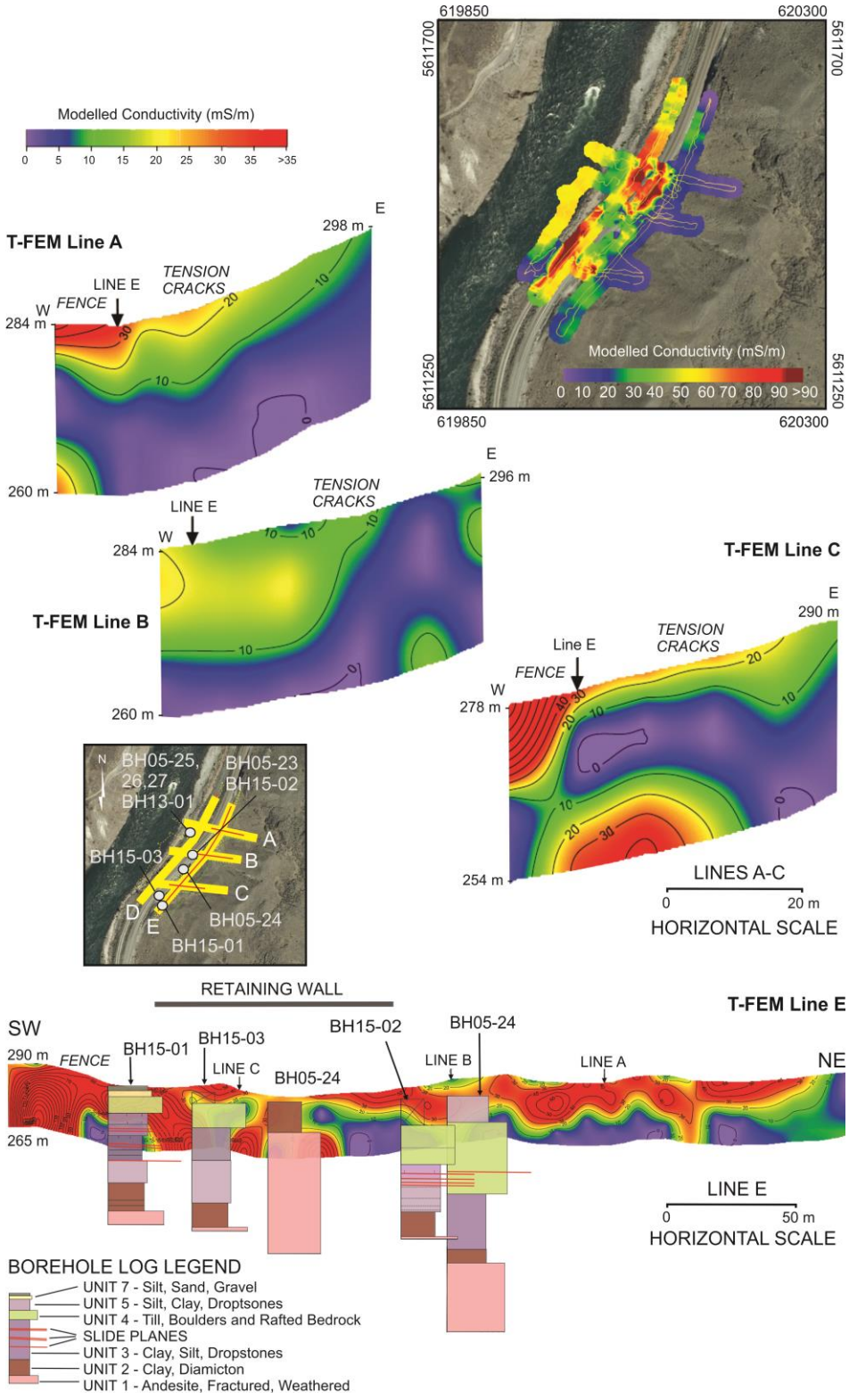

Figure 8 Combined T-FEM inverted profiles A-E and apparent conductivity plan mapl (after Parry et al., 2014); key features and lithologies are interpreted from field observations and graphic logs of boreholes BH15-01, BH15-02 and BH15-03 superimposed on profile Line E.

Poorly or imperfectly drained clay-silt (unit 3) and/or curvilinear landslide structures containing groundwater are interpreted at depths between 5 m and 15 m below the landslide surface (**Figure 8**). Clays (units 3 and 5) and water-saturated earth materials (units 7 and 9) are generally electrically conductive (red) and contrast sharply with more electrically resistive materials (green and blue) such as ballast (unit 10), gravels (units 7 and 9), till (unit 4) and bedrock (unit 1). Upslope of the CPR tracks (T-FEM Lines A-C; **Figure 3**; **Figure 8**), conductivities are 25 mS m^{-1} or less; indicating that in these areas, till (unit 4) and outwash (unit 6) are providing the bulk of the apparent conductivity response and are at least 3 to 4 m thick. These units minimize the influence of underlying, more conductive glaciolacustrine clay (units 3 and 5). To the west of T-FEM Line E, apparent conductivity values rapidly increase reflecting the reduction of thickness in the overlying till diamicton (unit 4) and the increasing proportion and thickness of glaciolacustrine clay and silt (units 3 and 5).

T-FEM Line A is the northernmost E-W cross-section and inverted EM results are shown in **Figure 8**. The dominant features on this profile are: a non-conductive (resistive) area at depth and up-slope corresponding to till (unit 4) and underlying bedrock (unit 1). Approaching T-FEM Line E and west, conductivity values increase reflecting the increased influence from the underlying glaciolacustrine clay. These readings correspond well to T-ERT measurements taken across this same area.

T-FEM Line B is the centre E-W cross-section. Plotted inverted T-FEM results (**Figure 8**) indicate non-conductive (resistive) areas at depth and up-slope corresponding to till diamicton (unit 4) and underlying bedrock (unit 1). West toward T-FEM Line E, conductivity values increase suggesting a greater influence from the underlying glaciolacustrine clay (unit 3). This effect is not as marked as with T-FEM Line A, reflecting a more extensive resistive material in general at depth.

T-FEM Line C is the southernmost E-W cross-section; and inverted T-FEM results are shown in **Figure 8**. The inverted FEM results on this line vary from the other east-west transect lines in that there appears to be three layers in the data. The results of these data indicate two relatively conductive areas between 10 and >30 mS/m on this profile: one near surface and the other at depth. Based on the surficial geology map (Huntley and Bobrowsky, 2014; **Figure 2**), these conductive areas are likely the glaciolacustrine clay (units 3 and 5). The middle layer is resistive with conductivities between 0 to 8 mS m^{-1}, suggesting a buried bedrock raft. This layering is consistently recorded by the three other terrestrial geophysical methods. Up slope, the more resistive areas are similar to T-FEM Lines A and B, and are a combination of till, colluviated gravel outwash (unit 8) and shallow bedrock. The seismic data for this survey line suggest a 'hidden' low velocity layer between two higher velocity layers. Layering is also indicated in the results of the T-ERT data where this line appears to have deeper bedrock with two possible layers. The T-FEM data suggest till overlying detached bedrock and glaciolacustrine clay. The T-GPR survey also shows multiple reflectors in this area (Parry et al., 2014).

T-FEM Line E is the one NE-SW cross-section. Inverted FEM results are shown in **Figure 8**. This line has higher conductivity values than the other three inverted T-FEM cross-sections due to the close proximity of a metal fence. Since the fence runs parallel to the dipole orientation, it has the potential to provide a significant conduction path influencing the EM34-3 results. This effect appears to be more significant on the southern side of the profile than the north. Despite this, the trends of the values recorded on this line agree very well with the recorded values of the intersecting E-W cross-sections. The inverted cross-section also agrees with the other geophysical results in that it suggests resistive till tapering out overlying glaciolacustrine clays with possible shallow bedrock at the southern end of the line (Parry et al., 2014).

3.3 Interpretation Terrestrial Ground Penetrating Radar Results

Terrestrial GPR lines A, B and C (**Figure 9a**) are divided into sections because of 'ringing' interference between steel rail tracks and the radar antenna. Boulder-rich clay deposits in the upper 5 m of all profiles generated pronounced reflections in an otherwise subdued datasets. Additionally, conductive clay absorbed much of the GPR signal, muting reflections from underlying units. A number of reflections have been identified in the GPR data and depths were calculated using a propagation velocity of 0.08 m ns^{-1} (average dielectric constant, K, of 14). This velocity is considered representative of both wetted sand and clay conditions (Parry et al., 2014). It is possible that the actual propagation velocity in till diamicton (unit 4) might be faster, in which case the velocity used could under estimate depths by as much as 20%. Reflectors with gentle slopes toward the valley axis likely indicate contrasts between clay and silt (units 3 and 5), coarser unconsolidated sediments (units 2, 4, 6 and 7), bedrock (unit 1) and groundwater-saturated earth materials at depths less than 40 m (**Table 2**).

Reflections cannot be seen in till (unit 4) because of the random, unsorted distribution of clasts in the diamicton matrix. Many boulders (erratics) were large enough to generate individual hyperbolic point reflectors and can be seen in the T-GPR data (**Figure 9**). Planar reflectors at different depths and at various inclined angles in the T-GPR profiles are seen on all lines and are interpreted to represent stratigraphic contacts and possible slide planes between bedrock and bouldery clay-rich surficial units. Stronger reflectors seen at depth in the upslope profiles roughly correlate with the resistive layers seen in the upper 10 m of the T-ERT data recorded in the same areas. It is likely this base reflector represents glaciolacustrine sediment (units 2 and 3) or bedrock contact (unit 1).

T-GPR Line A is the northernmost E-W cross-section (**Figure 9a**). A well-defined reflector can be seen on both line A and A2, appearing approximately 15 m below the ground surface up-slope and being within a couple of metres of the ground surface along the fence line. This reflector is likely a contact between the till diamicton (unit 4) and an underlying glaciolacustrine clay (unit 3). It is possible that the strength of the reflection is due to the presence of water accumulating along this boundary, increasing the reflection coefficient. Weaker reflections represent further minor lithological boundaries within and between the till diamicton (unit 4), glaciolacustrine (units 2 and 3) and andesite bedrock (unit 1). At the western most end of T-GPR Line A (**Figure 9a**), a number of reflective boundaries can be seen intersecting contacts within glaciolacustrine diamicton (unit 2) above bedrock (unit 1).

T-GPR Line B is the centre E-W cross-section (**Figure 9a**). Reflections show similar patterns to T-GPR Line A, but are deeper and fainter. This is attributed to increased attenuation in the surface layer due to greater travel distances and possibly higher fines contents and/or lower water content contrasts at the lithological boundaries (Parry et al., 2014). T-GPR Line C is the southernmost E-W cross-section (**Figure 9a**). Near the head of the landslide, a relatively strong reflective feature between 12 and 20 m depth is evident. This reflector is also captured by the T-ERT and seismic refraction surveys, and represents a conductive layer sandwiched between deep competent bedrock and a resistive layer on the surface (Parry et al., 2014).

T-GPR Line D is the westernmost NE-SW cross-section (**Figure 9b**). This line does not intersect rail lines, so there is no interruption in the data coverage. However, due to the proximity to the CN rail track, there is 'ringing' in the data due to interference with the steel rails and the radar antenna. There are a number of gradually sloped reflectors, the orientation of which may indicate past or current landslide activity. Line E is the centre NE-SW cross-section (**Figure 9b**). Since rail tracks do not intersect this cross-section, there is no interruption in the data coverage. There are a number of gradually sloped reflectors that possibly indicate past or current landslide activity. T-GPR Line F, the easternmost NE-SW cross-section does not intersect the rail tracks (**Figure 9b**), but runs slightly upslope of the other lines and shows fewer gradually sloped reflectors than lines D and E (Parry et al., 2014).

3.4 Interpretation of Terrestrial Seismic Refraction Results (P-Wave Velocities)

Good seismic velocity contrasts were observed between the surficial units and underlying bedrock (Parry et al., 2014). The five terrestrial SR lines agree relatively well with each other at the five intersection points (**Figure 10**). Variations are attributed to lithological layers pinching out at right angles to the profile line and 2D modeling inaccuracies (Parry et al., 2015).

Along the five seismic refraction lines, sub-surface stratigraphic boundaries, different earth materials and other features (e.g., groundwater table) were identified from the refraction of acoustic energy provided by stacked ground-blows using the sledgehammer. The seismic refraction survey provided detailed information on the distribution and thicknesses of subsurface layers with characteristic seismic velocities. Till diamicton (unit 4), colluvial diamictons (units 2 and 8), sand and gravel (unit 6), silt and clay (units 3 and 5), competent bedrock (unit 1), groundwater conditions and water table are all observed in refraction profiles (**Figure 10**).

Seismic (P-wave) velocities recorded vary from 246 m s^{-1} on the surface to >3500 m s^{-1} at depth (**Table 2**). Velocity ranges in unconsolidated units are more a function of internal structures, compaction, density and water content rather than type of subsurface material. P-wave velocities less than ~1200 m/s implies that bedrock and overlying deposits are above the water table and not fully saturated. The refraction of P-waves along valley-dipping reflectors (e.g., bedding and slide planes observed in the field and borehole logs, see Section 5.1) may also account for the wide range in values. Velocities between 246 m s^{-1} and 600 m s^{-1} (blue on cross-sections) correspond to loose material within colluviated outwash and scree (unit 8) and ballast beneath the rail tracks

(unit 10). Velocities between 400 and 2300 m s^{-1} (yellow and green on cross-sections) represent more compact till (unit 4) and glaciolacustrine clays (units 2, 3 and 5); and velocities of >3500 m s^{-1} (orange and red on the cross-sections) are indicative of bedrock and weathered regolith (unit 1) and glaciolacustrine materials (units 2 and 3) underlying alluvial floodplain deposits (unit 9) at the landslide toe (Parry et al., 2014).

Seismic Refraction (SR) Line A, the northernmost E-W cross-section (**Figure 10a**), begins west of the CN rail tracks and ends 155 m up-slope to the east. Low seismic velocities recorded near the surface (more so than other lines) are likely due to loose material (units 4 and 8) in the upper 10 m related to the abundant tension cracks and slide scarps along SR Line A. The highly resistive layer seen in the upper 7 m of the T-ERT Line A is related to the low velocity layer between 200 m s^{-1} to 2500 m s^{-1} observed in the upper 6 m of the seismic data. This material is most likely till diamicton (unit 4). Elevated velocities (>3500 m s^{-1}) between 11 m and 20 m depth correlate with depressions in resistivity observed in the same area on the T-ERT survey (see above, Section 3.1), and resistivity most likely indicate buried depressions and ledges in bedrock infilled with colluvium and till.

SR Line B is the centre E-W cross-section (**Figure 10a**), and begins directly west of the CN rail tracks and ends 155 m up-slope to the east. Open tension cracks were observed on and around this survey line east (i.e., up-slope) of the CPR tracks. A highly resistive layer observed in the upper 9 m in the T-ERT data is most likely related to the low velocity layer observed in the upper 8 m of SR Line B. This material is most likely till diamicton (unit 4) or loosely consolidated gravel-rich colluvium derived from glaciofluvial outwash (unit 8). Drops in velocity (below 3500 m s^{-1}) correlate with resistivity lows in the same area on the T-ERT survey; and most likely indicate bedrock depressions and ledges infilled with unconsolidated earth materials (units 2 and 4).

SR Line C, the southernmost E-W transect (**Figure 10a**) begins directly west of the CPR tracks and ends 155 m up-slope to the east. Seismic velocities are similar to the other E-W transect lines, and increase to >3500 m s^{-1} at depth and correlates with field observations along this line. Travel time curves for this line show evidence of a possible 'hidden' or 'blind' seismic low velocity layer, interpreted as a possible slide plane (Parry et al., 2015).

SR Line D is the westernmost NE-SW cross-section (**Figure 10b**). Ground conditions allowed all 48 geophones to be placed, resulting in significantly less noise and better data quality on this line compared to cross-sections up-slope. Along the southernmost part of this line, high seismic velocities (>3500 m s^{-1}) were observed at 11 m depth rising northward along the cross-section to approximately the intersection with line D, suggesting south-dipping bedrock in this location. In centre, higher seismic velocities (>3500 m s^{-1}) reach 9 m to 17 m depth before deepening along the northern section of the line. The velocity ranges support the current stratigraphic model that suggests ballast (unit 10) overlies alluvial sand, gravel, boulders (unit 9), till diamicton (unit 4), glaciolacustrine clay and diamicton (units 2 and 3) and bedrock (unit 1).

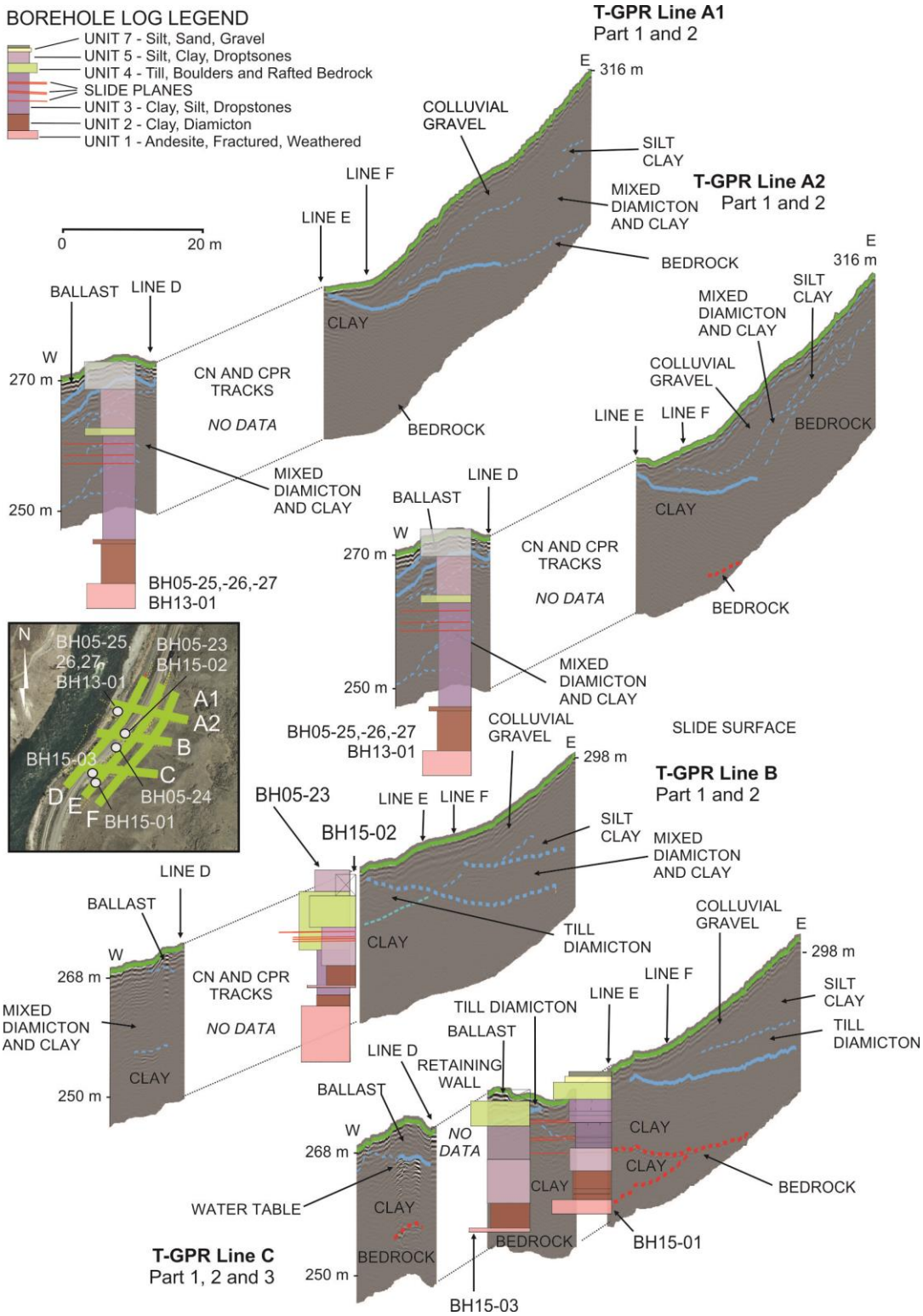

Figure 9 a) 50 MHz T-GPR Lines A-C; red dotted line - strong reflector; blue solid line – moderate reflector; blue dashed line – weak reflector; lines A1 and A2 lie parallel on the slope and are 5 m apart (after Parry et al., 2014); key features are interpreted from field observations and graphic logs of boreholes BH15-01, BH15-02 and BH15-03 superimposed on profiles.

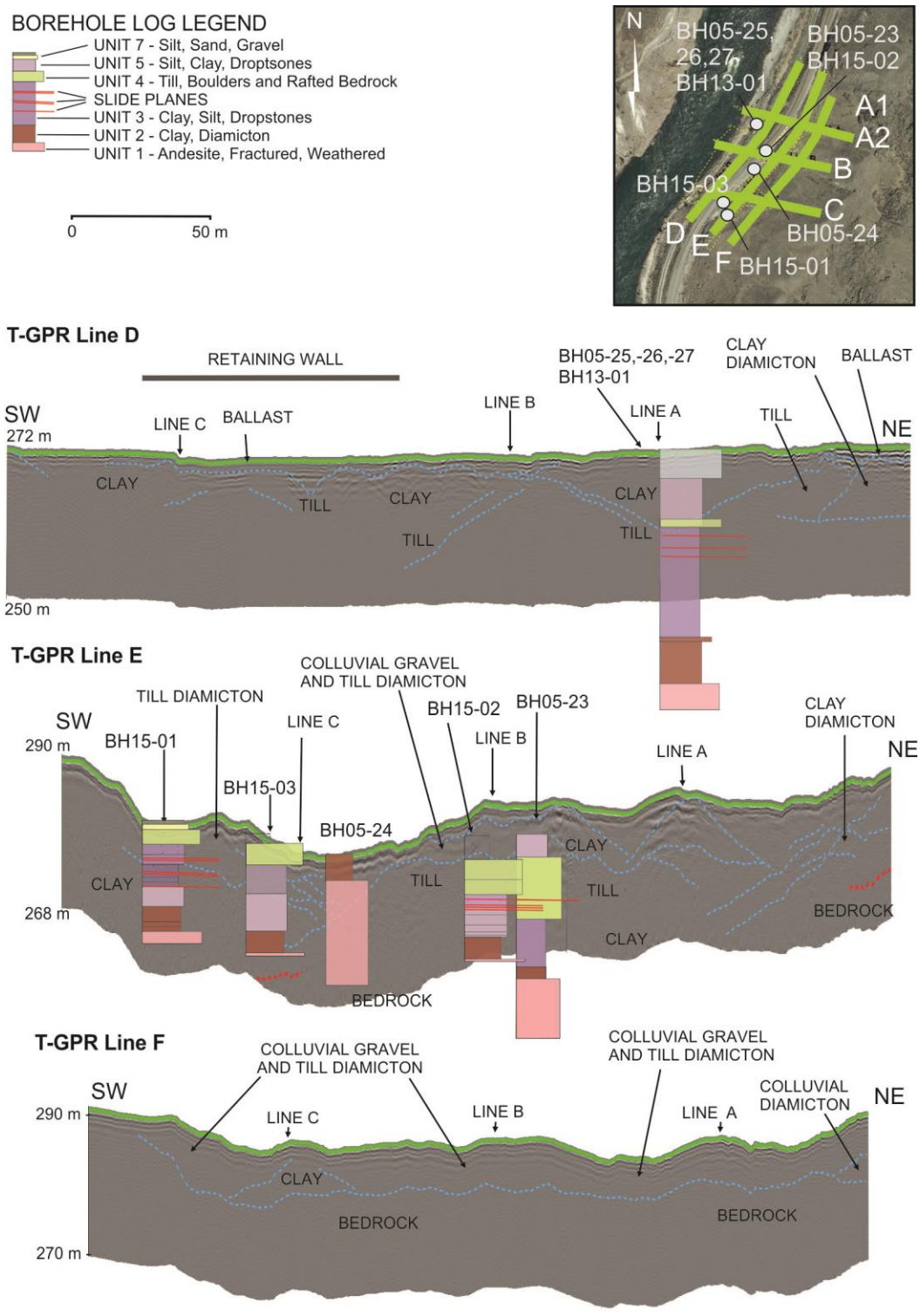

Figure 9 b) T-GPR Lines D-F; red dotted line - strong reflector; blue solid line – moderate reflector; blue dashed line – weak reflector (after Parry et al., 2014); key features are interpreted from field observations and graphic logs of boreholes BH15-01, BH15-02 and BH15-03 superimposed on profiles.

.

SR Line E is the easternmost NE-SW cross-section (**Figure 10b**). Ground conditions also allowed all 48 geophones to be placed; however, there were issues with noise because of loose colluvial materials (unit 8) at the surface. In the south, high velocities (>4000 m s^{-1}) were observed at a lower elevation than any other part of the line (15 m depth). Northward, the elevation of the 4000 m s^{-1} contour line marking the bedrock-surficial material boundary varies between 4 m and 9 m depth (**Figure 10b**).

3.5 Interpretation of Terrestrial Multispectral Analysis of Shear Wave Results

The terrestrial MASW results for SR lines A-E illustrate a general increase in velocity with depth. The areas of thick overburden located at lower elevations and over the western half of the site area are clearly delineated by lower shear wave velocities. Along SR lines D and E, a surface to near-surface low shear wave velocity layer ranges from 130 m s^{-1} to 350 m s^{-1} with an average thickness of approximately 10 m (**Figure 10b**). The low velocity layer thins to the east from a thickness of 14.5 m along the CN tracks to 0 m at the eastern ends of SR lines A and C, coincident with an increase in ground elevation (Gugins and Candy, 2015). This layer corresponds to borehole intersections of silt and clay with some boulders (unit 4).

Underlying this low velocity layer, shear wave velocities increase to values of 450 m s^{-1} to 600 m s^{-1} (**Figure 10b**), corresponding to the onset of denser subsurface materials (units 2 and 3). These velocities are consistent with nearby borehole intersections of stiff clay, stiff to hard clay, silty clay, and silty to sandy clay. Beneath this dense layer, the shear wave velocities increase to a range of 550 m s^{-1} to 700 m s^{-1} (**Figure 10b**). These values are consistent with the weathered fractured and weathered Andesite (unit 1) encountered at the base of boreholes BH15-01, BH15-02 and BH15-03.

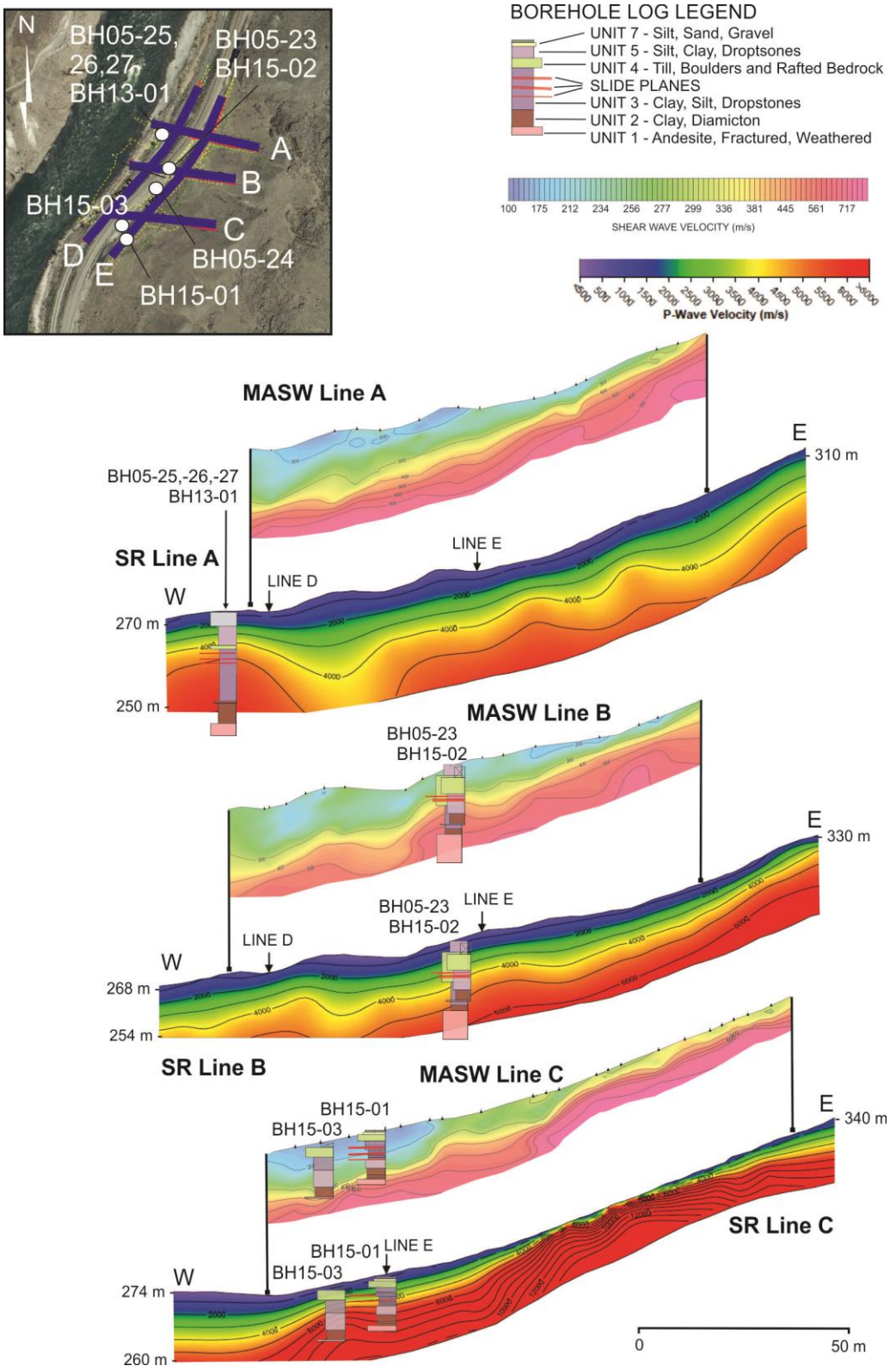

Figure 10a MASW and SR lines A-C pseudosections (after Parry et al., 2014; Gugins and Candy, 2015); graphic logs of boreholes BH15-01, BH15-02 and BH15-03 are superimposed on profiles.

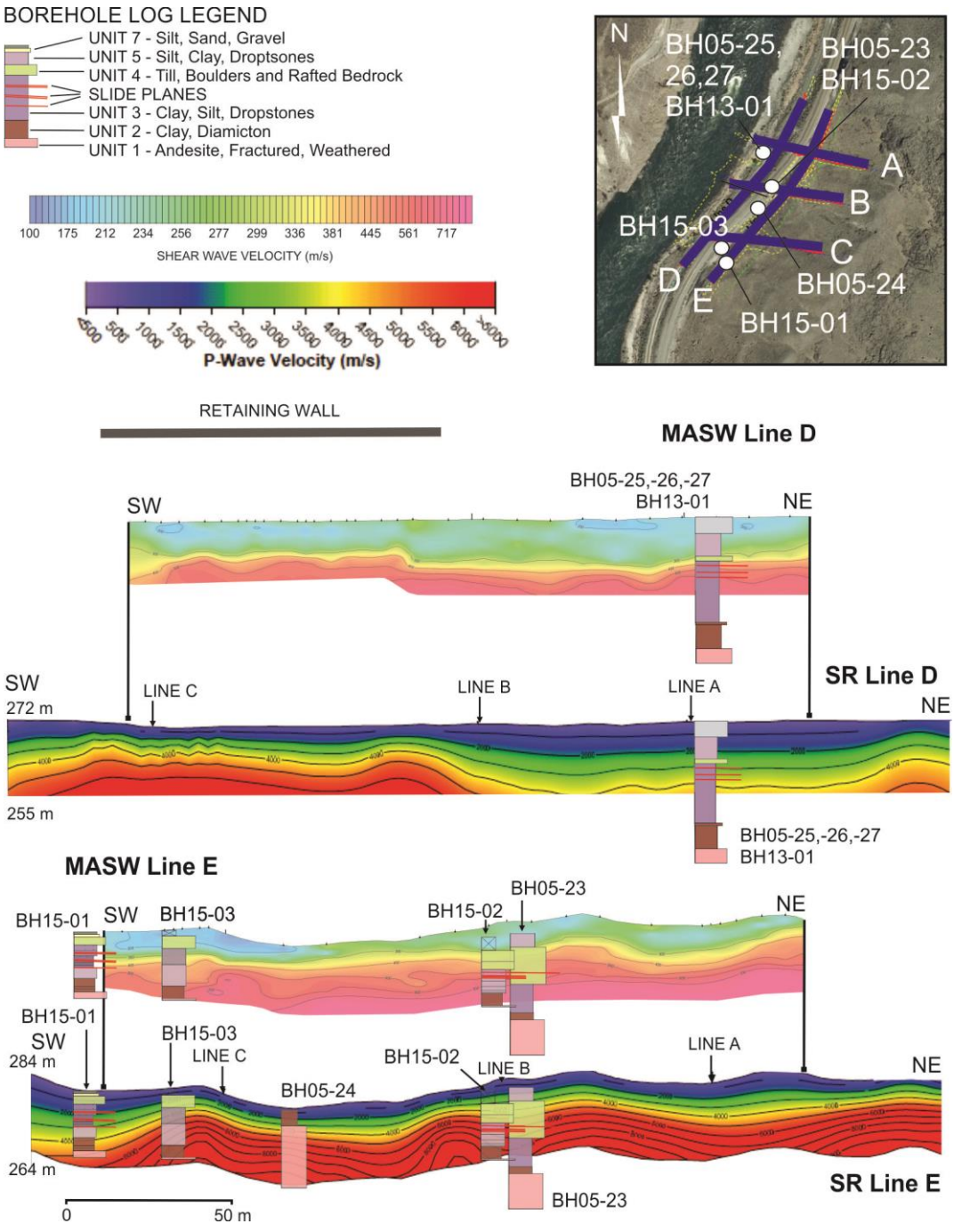

Figure 10b MASW and SR lines D-E pseudosections (after Parry et al., 2014; Gugins and Candy, 2015); graphic logs of boreholes BH15-01, BH15-02 and BH15-03 are superimposed on profiles.

4. Waterborne Geophysics Results and Interpretation

Waterborne geophysical surveys provide new insight into the sub-surface bottom thickness of earth materialssediments and depth to bedrock; groundwater conditions, resistivity, conductivity and failure mechanisms of the landslide.

4.1 Interpretation of Acoustic Bathymethry Results

An average river elevation of 264.5 m above sea level (masl) was derived from the acoustic bathymetric (AB) survey line paths (for November 19, 2014). For the reach of Thompson River surveyed, river bottom elevation data were subtracted from this elevation to get river bottom elevations. Gridded elevation data generally shows shallow water along the eastern and northern portion of the surveyed reach; and deeper water along the steep western bank and southern portion of the surveyed reach (**Figure 11a**).

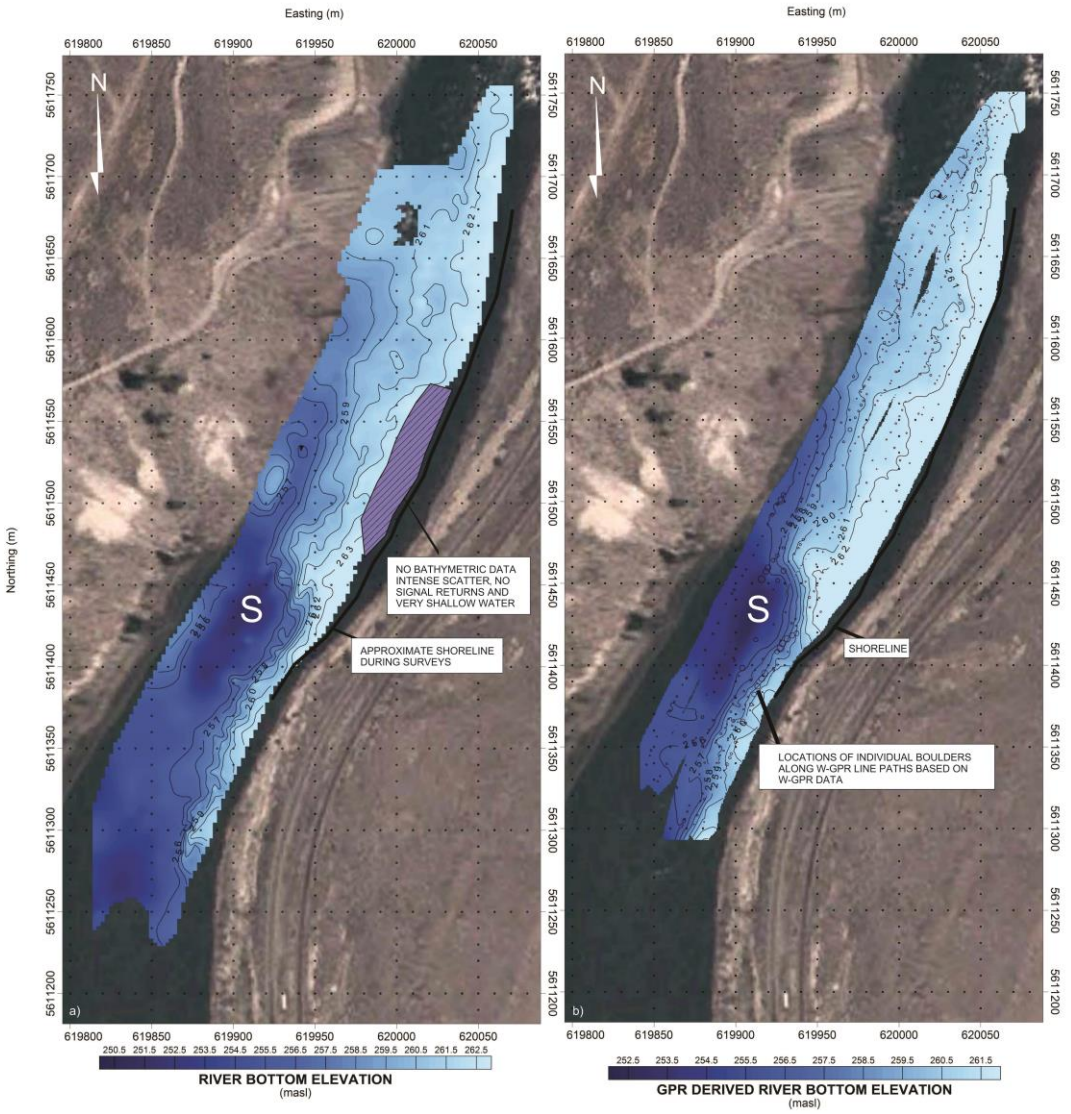

Figure 11 a) Acoustic based river bottom elevation; b) W-GPR river bottom elevation with boulder locations; S – scour pool (after Bauman et al., 2015).

River bottom elevations ranged from approximately 251.3 m asl to 263.8 m asl. The convex form of the submerged channel revealed in the bathymetry results suggests the landslide toe extends beneath the Thompson River. Strongest currents flow above a >10 m deep trough along the left bank and through a >15 m basin in the SW interpreted as a scour pool (Bauman et al., 2015). The location of this latter submerged erosional feature strongly suggests river incision is driving the higher rates of movement observed over the south part of the landslide.

In the middle of the surveyed reach, bathymetry data could not be collected near the left bank because large boulders caused scatter in the return signal and the water was too shallow to safely navigate. Bathymetry derived from the W-GPR data shows shallower water toward the eastern riverbank (**Figure 11b**).

4.2 Interpretation of Waterborne Electrical Resistivity Tomography Results

Of the seven W-ERT survey lines collected, four datasets were processed due to their higher signal quality and reduced noise (W-ERT Line 2, W-ERT Line 3, W-ERT Line 4 and W-ERT Line 5; **Figure 3**). Discussion of the processing and inversion techniques used (Bauman et al., 2015) lies outside the scope of this report. Due to the fast currents and rapids, the datasets were edited to remove noisy data points resulting from poor contact with the water surface. Electrode positions can still be observed on W-ERT profiles. Each survey line was collected going upstream for optimal survey speed and control. The locations of the W-ERT lines are shown in **Figure 3** and **Figure 12**. Similar to T-ERT results, waterborne resistivity values are higher for sand, gravel and diamicton (units 2, 4, 8 and 9), and lower for clay and silt (units 3 and 5). Small amounts of fine to coarse-grained sediment (such as sand beds and dropstones) can alter the resistivity of unit 2 making it electrically more conductive. Conversely, unsaturated sand and gravel can elevate the bulk resistivity of otherwise conductive clay-rich diamicton till (unit 4). Pore-water will also affect the resistivity of a unit, with high salinity water reducing the resistivity of a unit. Magnetite- and ilmenite-bearing andesite (unit 1) is very resistive, although this can vary depending on weathering, jointing, and fracturing in the bedrock (Parry et al., 2014; Bauman et al., 2015; Gugins and Candy 2015).

W-ERT Line 2 was collected on a southwest to northeast trend, and is approximately 358 m long (**Figure 12**). A large high resistivity zone (exceeding 1,000 Ωm; pink colours) has been imaged between approximate line stations 60 m and 225 m. The resistivity values exceed 3,000 Ωm in many portions of this zone. The low resistivity layer (less than 25 Ωm; dark blue colours) extends across much of the section. Intermediate resistivity values (ranging between 100 Ωm and 450 Ωm; green colours) are found near the river bottom and near the bottom of the section (Bauman et al., 2015). The high resistivity zone is thought to be associated with andesitic bedrock (unit 1), given its very high resistivity values that contrast greatly with the surrounding low resistivity (dark blue) values. The latter are thought to be primarily fine-grained materials such as silt and clay (unit 3), diamicton (unit 4) and groundwater. W-GPR diffraction patterns indicate interstitial boulders are located throughout this layer and may represent rock fall blocks from the cliff (unit 8) or glacial erratics within till diamicton (unit 4). A potential block of high resistivity igneous rock is also denoted in **Figure 12** between line stations 60 m and 90 m. Intermediate resistivity

values (green colours) imaged near the river bottom are interpreted to be associated with modern fluvial deposits of gravel, cobbles and boulders (unit 9).

W-ERT Line 3 was also collected on a southwest to northeast trend, and is approximately 490 m long (**Figure 12**). A large high resistivity zone has been imaged with confidence between approximate line stations 140 m and 260 m, with values exceeding 3,000 Ωm in many portions. It is interpreted to be andesitic bedrock (unit 1). A potential block overrides the *in situ* andesite between line stations 150 m and 205 m. This possible capping block is interpreted largely due to the odd mushroom shape. Another potential block is denoted on **Figure 12** at line station 230 m. Much like W-ERT Line 2, the low resistivity layer (dark blue) is interpreted to be associated with fine-grained sediments (units 3 and 4), potentially containing groundwater. Intermediate resistivity (greens) imaged near the river bottom corresponds to coarse-grained sediment such as gravel, cobbles and boulders (Bauman et al., 2015).

W-ERT Line 4 and W-ERT Line 5 are 103 m and 175 m long, respectively, and trend southwest to northeast (**Figure 12**). Both sections show similar layering/resistivity zones to W-ERT Line 2 and W-ERT Line 3, but with the absence of the high resistivity zone thought to be bedrock. Top of bedrock could potentially be deeper than the waterborne ERT depth of investigation on W-ERT lines 4 and 5. It is also possible that the intermediate resistivity values near the bottom of the sections (especially in W-ERT Line 5) may indicate heavily weathered or fractured bedrock (Bauman et al., 2015). Potential igneous blocks and river bottom coarse-grained sediments have been noted on the sections (**Figure 12**).

4.3 Interpretation of Waterborne Electromagnetic Induction Results

Factors that affect two dimensional (2D) resistivity data also influence EM31 terrain conductivity data (grain size, water saturation, and pore water conductivity). Specifically for this survey, mapping locations of pore water discharge with a differing conductivity than river water was a high priority. The waterborne EM31 survey was conducted in November 2014, with all survey lines collected while travelling downstream in the raft. The results are displayed as gridded data over the river bottom elevation contours (**Figure 13**). In addition to the W-EM31 data, two subparallel terrestrial survey lines were collected on the east bank as close to the water as safely possible. All EM31 terrain conductivity data are corrected to account for the river water depth assuming a one-dimensional (1D) two-layer model of water over sediments, and a 6 m penetration depth for the EM31 signal (cf. Butler et al., 2004; Bauman et al., 2015). Without the bathymetric corrections, the W-EM31 conductivities are heavily influenced by the conductivity of the water column, and the EM31 data are a muted mimic of the bathymetry (**Figure 11a, b**; **Figure 13a**).

W-EM31 terrain conductivity values corrected for water depth range from approximately 4 mS m^{-1} to 68 mS m^{-1} (**Figure 13b**). Three zones labelled A, B, and C show elevated terrain conductivity values which exceed 60 mS/m. These elevated values could be associated with buried fine-grained sediments (units 3 and 4) containing groundwater. If bathymetry data could have been successfully collected closer to the eastern shore, allowing for near-shore W-EM31 terrain conductivity data to be bathymetry corrected, other elevated EM31 terrain conductivity

zones may have been mapped. This hypothesis is based on the inverse relationship between water depth and corrected EM31 data, along with the observations that water depths are generally shallow closer to the eastern shore, and that the uncorrected W-EM31 terrain conductivity data (**Figure 13a**) display relatively high values near the eastern shore (Bauman et al., 2015).

4.4 Interpretation of Waterborne Ground Penetrating Radar Results

The locations of waterborne GPR cross-sections are shown in **Figure 3**. The minimum and maximum line lengths are 383 m (W-GPR Line 4) and 541 m (W-GPR Line 9), respectively (**Figure 14a-c**). Many boulder diffractions are visible in the W-GPR cross-sections, and some boulder diffractions located on the riverbed are annotated on the cross-sections (**Figure 14a, b, c**). Secondary events or multiple reflections (multiples) are evident on most of the W-GPR cross-sections (W-GPR lines 5 through 10) as the laterally continuous reflectors at depth (**Figure 14b, c**). These are a function of multiple reflections off the river bottom and water/air interface (Bauman et al., 2015). No obvious stratigraphy, sedimentary structures or sediment packages can be interpreted on the W-GPR cross-sections due to the boulder diffractions in the modern fluvial sediments (unit 9). At the southern end of the GPR lines, in the vicinity of the large resistive zones identified in the W-ERT, radar velocities do not indicate competent bedrock, due to the apparently high water content reducing the velocities. The W-GPR data in this area indicate thick granular overburden with slower velocities with much diffraction (unit 9) rather than igneous bedrock (unit 1) where higher radar velocities would be expected Bauman et al., 2015).

While this is an apparent contradiction with the W-ERT data in this area, it is likely that the W-GPR is imaging bedrock (unit 1) due to the correlation with relatively high velocity seismic data (Parry et al., 2014; Gugins and Candy, 2015). Surface boulders under individual W-GPR survey line paths are displayed in **Figure 11b**. The largest boulders are located in the southern portion of the survey area where deeper bathymetry is recorded and shallow, high subsurface W-ERT resistivity zones are identified (Bauman et al., 2015; **Figure 12**)

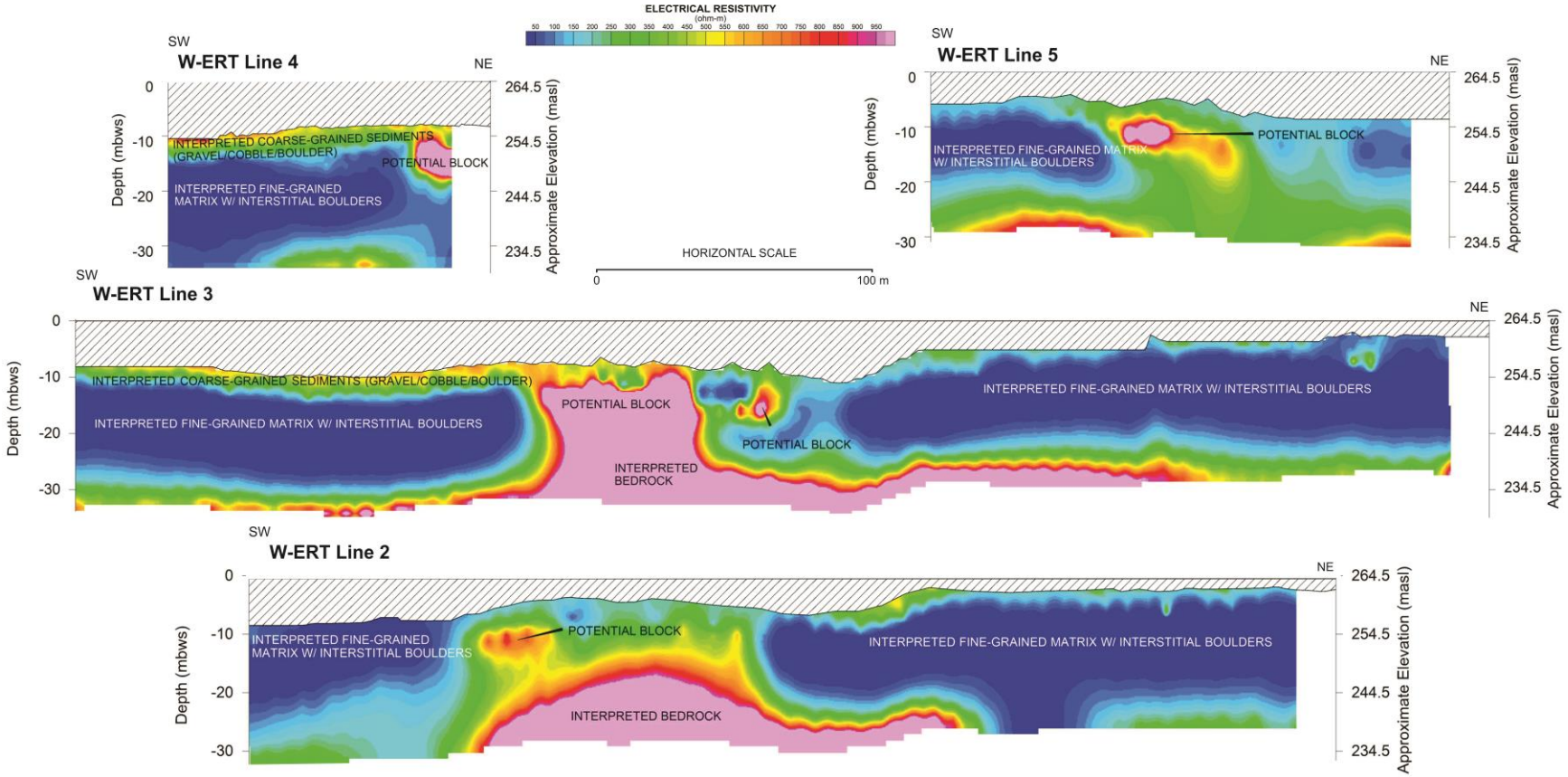

Figure 12 2D resistivity models of the subsurface along W-ERT lines 2-5; with interpretations based on field observations at the Ripley Landslide (after Bauman et al., 2015); see **Figure 3** for location of W-GPR cross-sections.

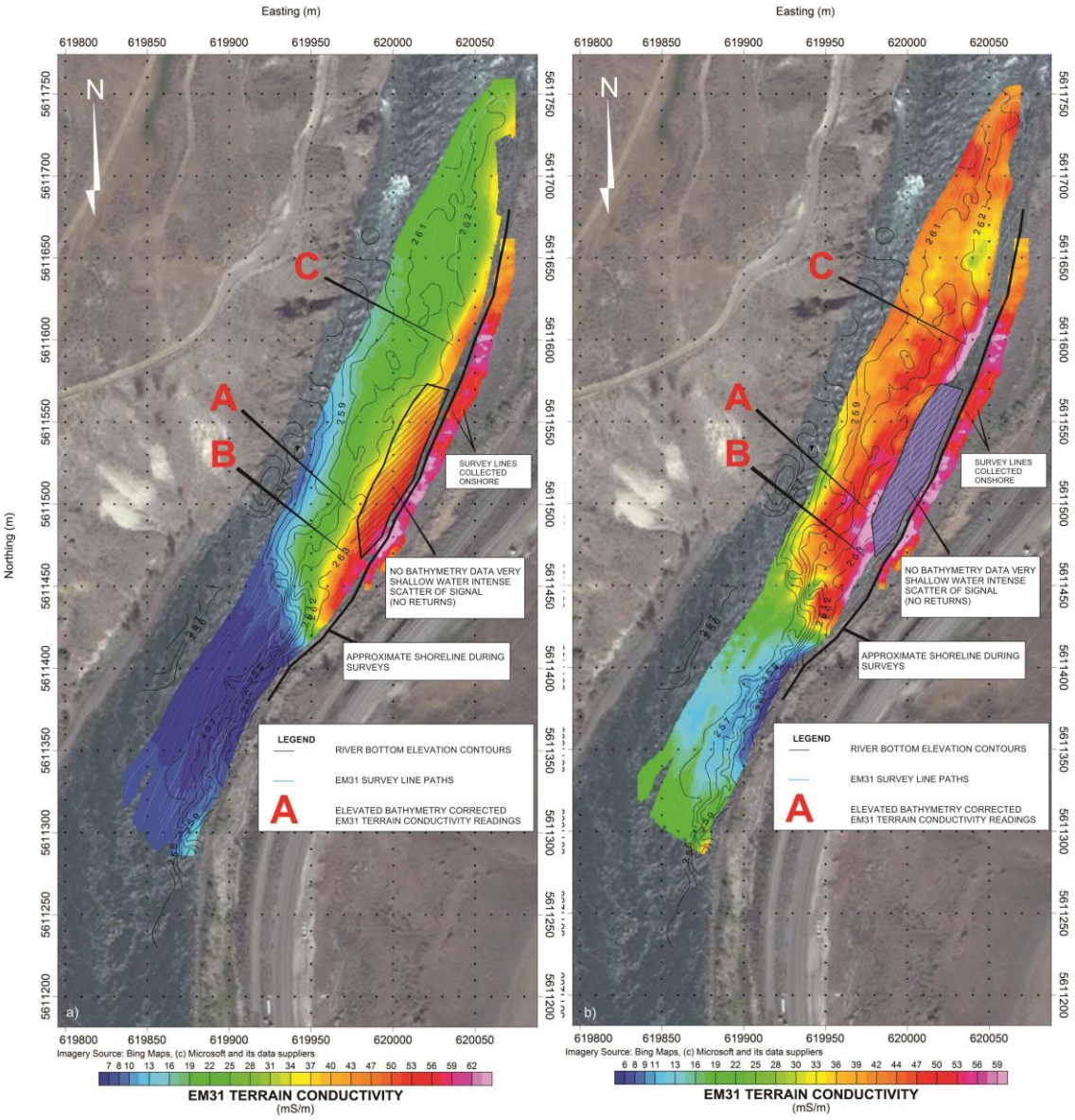

Figure 13 a) W-EM31 terrain conductivity data, uncorrected for bathymetry; b) Bathymetry corrected W-EM31 terrain conductivity data, showing areas with elevated conductivity, A-C. Due to the absence of bathymetry data in certain areas, portions of the W-EM31 data could not be corrected for water depth, and these data are not displayed (after Bauman et al., 2015).

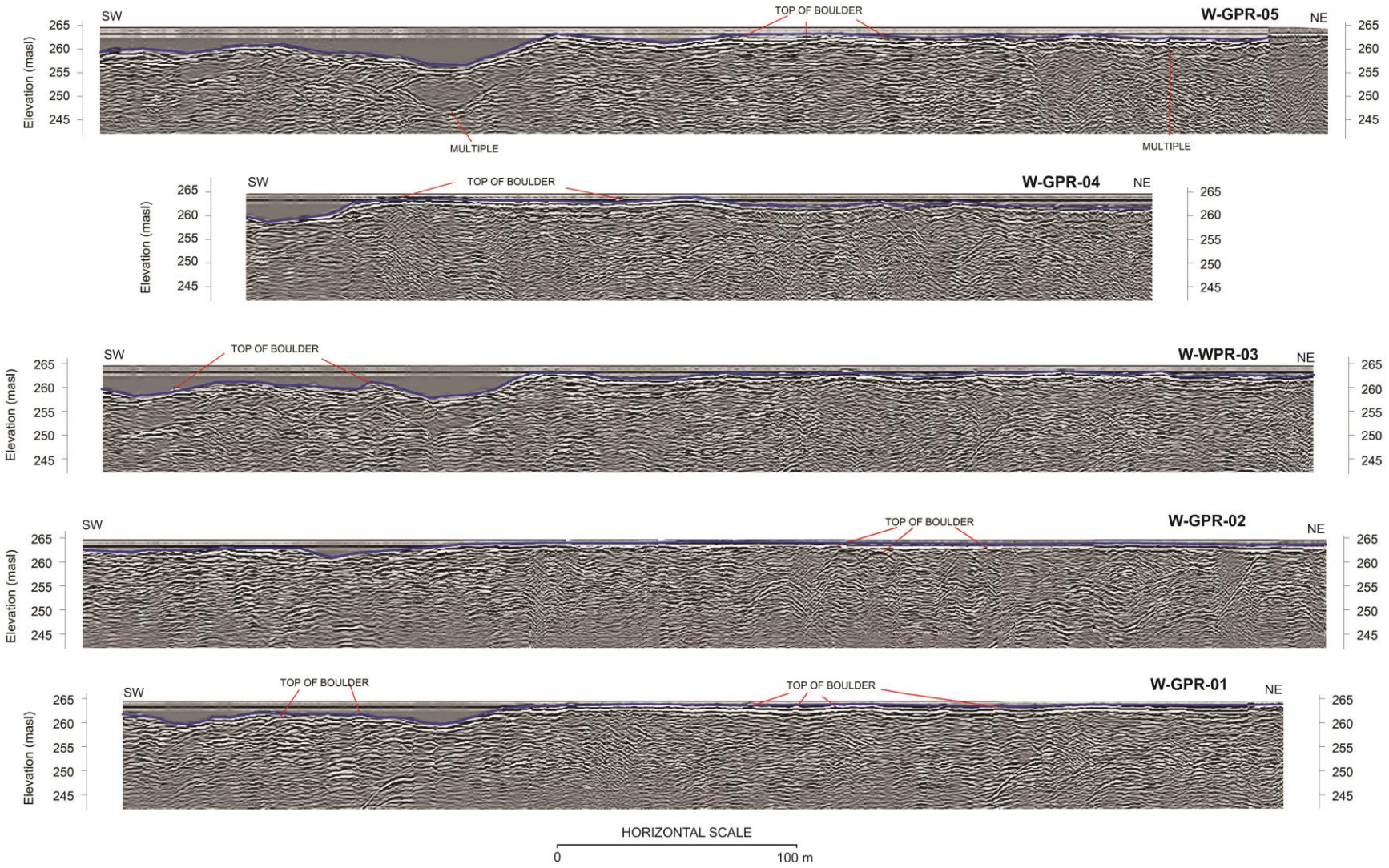

Figure 14a W-GPR Lines 1-5, with interpretations of subsurface earth materials and structures based on field observations at the Ripley Landslide (after Bauman et al., 2015); see **Figure 3** for location of W-GPR cross-sections.

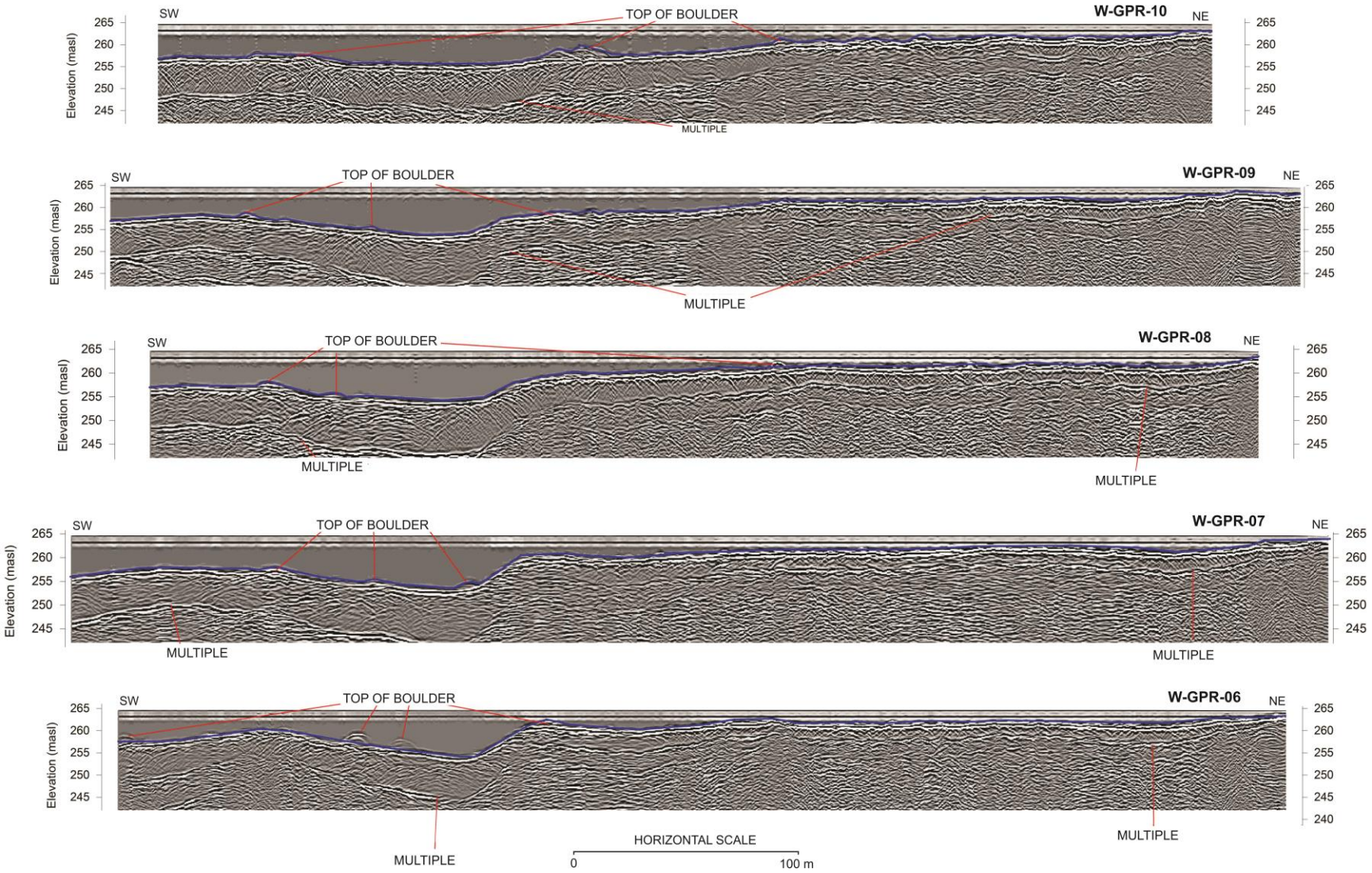

Figure 14b W-GPR Lines 6-10, with interpretations of subsurface earth materials and structures based on field observations at the Ripley Landslide (after Bauman et al., 2015); see **Figure 3** for location of W-GPR cross-sections.

5. Borehole Geophysics Results and Interpretation

The focus here is on the description and interpretation of boreholes completed in 2015: BH15-01, BH15-02 and BH15-03 (**Figure 2**; **Figure 3**; **Figure 6a**). Downhole surveys of natural gamma radiation levels, conductivity, and magnetic susceptibility provide further insight into the sub-surface thickness of earth materials, depth to bedrock, groundwater conditions and failure mechanisms of the landslide.

East of the CPR tracks, the logging tool encountered 15 m to 17 m of glacial deposits overlying basal bedrock in boreholes BH15-01, BH15-02 and BH15-03 (**Figure 15**). West of the CN tracks, BH05-25, BH05-26, BH05-27 and BH13-01 show around 30 m of consolidated till and clay-rich glaciolacustrine sediments overlying bedrock (**Figure 2b**). These observations corroborate the terrestrial and waterborne geophysics results indicating the main landslide body is located over a >20 m deep bedrock basin underlying the modern Thompson River.

The subdued variation in natural gamma responses (GR) of glacial deposits and bedrock indicates little variation in the lithological composition and grain-size characteristics in the surveyed boreholes (**Figure 15**). When compared to sediment logs, counts are generally more elevated in finer grained sediments (clay and silt beds) and reduced in coarser grained sediments (boulder, sand and gravel beds). Surface observations of granitic and arkosic dropstones in glaciolacustrine units (units 2 and 3) and erratics in till (unit 4) suggest a source for minor peaks of elevated counts. For glacial sediments (i.e., units 2 to 5), only a small fraction of the totals counts per second (perhaps 1 or 2 in 40) are likely from decaying Uranium, Thorium and Potassium isotopes (Gugins and Candy, 2015).

Induction Conductivity (IC) measurements were unaffected by borehole fluids and the presence of the plastic casing. The combination of large conductivity range, high sensitivity and very low noise and drift allowed accurate measurements of subsurface conditions (Gugins and Candy, 2015). During repeat runs up and down hole, the logs were repeatable. The resulting conductivity logs indicate that subsurface units are difficult to distinguish since they do not show strong contrasts (dynamic range ~5 to 25 mS/m). Similar to the GR data, this indicates similarities in lithological composition of sub-surface units. It is difficult to distinguish thick and less conductive layers from less thick, more conductive layers without reference to the borehole sedimentary logs (**Figure 15**). The amount and distribution of groundwater, and the presence of clay minerals with conductive ion-exchange properties determine the bulk electrical conductivity within sediment and bedrock units.

Magnetic susceptibility (MS) logs show that the subsurface units and bedrock contain very low amounts of ferromagnetic minerals (e.g., magnetitite, ilmenite and pyrrhotite). The magnetic susceptibility response allowed for accurate measure of earth materials surrounding the three boreholes to a distance of approximately 25 cm (Gugins and Candy, 2015).

Combined, these results are important for the interpretation of the terrestrial and waterborne ERT and EM profiles, since they confirm that the boundaries between units are gradational (not sharp), and fall within a narrow range typical of glacial sediments.

5.1 Interpretation of Borehole Geophysics Results

Borehole BH15-01 is located off the active landslide, 50 m from the southwest end of terrestrial geophysics survey Line E, 20 m southwest of terrestrial survey Line C and approximately 15 m southeast of BH-03 (**Figure 2**, **Figure 6a**). The borehole was drilled into a relict back-tilted slide block that is now partly buried by alluvial silt (unit 7). The natural gamma log shows minor fluctuations around a background level response of 35 cps. The sediment column, from a nuclear point of view, is pretty uniform, although minor peaks might be attributed to the presence of clay, sand beds, granitic erratics and dropstones in units 2, 3 and 4 (**Figure 15a**).

The uppermost 0.9 m of both the conductivity and magnetic susceptibility logs record the base of the steel stick-up and are not plotted (**Figure 15a**). Small deviations in the conductivity log are likely reflecting changes in grain size within units 2, 3 and 4. A relatively high conductivity zone (20 mS m^{-1}) centred near 2.2 m below surface coincides with till diamicton containing clay, silt and boulders (unit 4); and possibly an increase in groundwater content at this depth. Underlying this relative high is a broad, lower conductivity zone (<10 mS m^{-1}) that extends to 6.5 m, corresponding to underlying clay containing cobbles (dropstones) and silt and sand beds (unit 3). A slight rise in conductivity is coincident with logged fissures near 5.1 m and may indicate an increase in water content at this depth. From 6.5 m to 12 m, conductivities show moderate values (around 18 mS m^{-1}) consistent with silt and clay (unit 3). Fissures near 7.5 m and 9 m are not represented in the conductivity readings, suggesting low water content at these depths. These structures are either related to current landslide movement and are sub-horizontal slide planes; or they are relict glaciotectonic structures related to the overriding of glacial lake deposits by ice during the last glaciation. From 12 m to 17 m, conductivity values fluctuate from low to moderate (12 mS m^{-1} to 18 mS m^{-1}) in the presence of a mixed diamicton containing clay, silt, pebbles and cobbles (unit 2) overlying weathered and fractured andesite (unit 1). The magnetic susceptibility log has a similar character to the conductivity log, although the features are more subdued (**Figure 15a**). An average MS response of approximately 0.25 ppt suggests units 2, 3 and 4 contain low concentrations of ferromagnetic minerals.

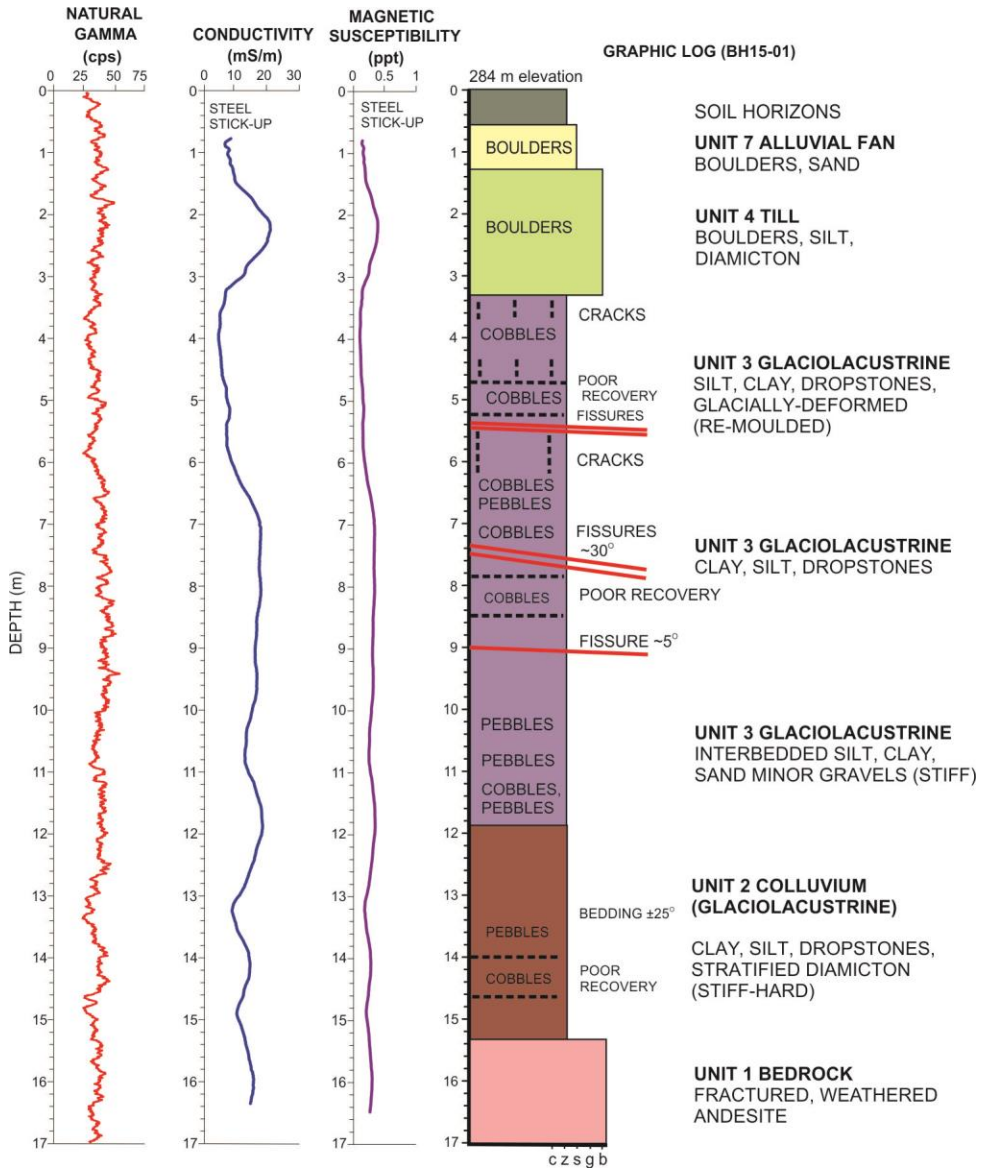

Figure 15a Natural gamma, conductivity and magnetic susceptibility results plotted and graphic log profile for BH15-01; see **Figure 2** and **Figure 6a** for location (after Gugins and Candy, 2015); grain sizes, c – clay; z – silt; s – sand; g – pebbles, cobbles; b – boulders.

BH15-02 is located east of the CPR tracks near the centre of terrestrial geophysics survey Line B and 5 m west of terrestrial survey Line E (**Figure 2**, **Figure 6a**). The natural GR log shows a relatively constant response at approximately 40 cps for the majority of the borehole (**Figure 15b**). This suggests low concentrations of U, Th and K within the clay-rich units intersected in the hole. Minor peaks can be attributed to the presence of granitic and arkosic dropstones, erratics and sand layers in units 2, 3 and 4.

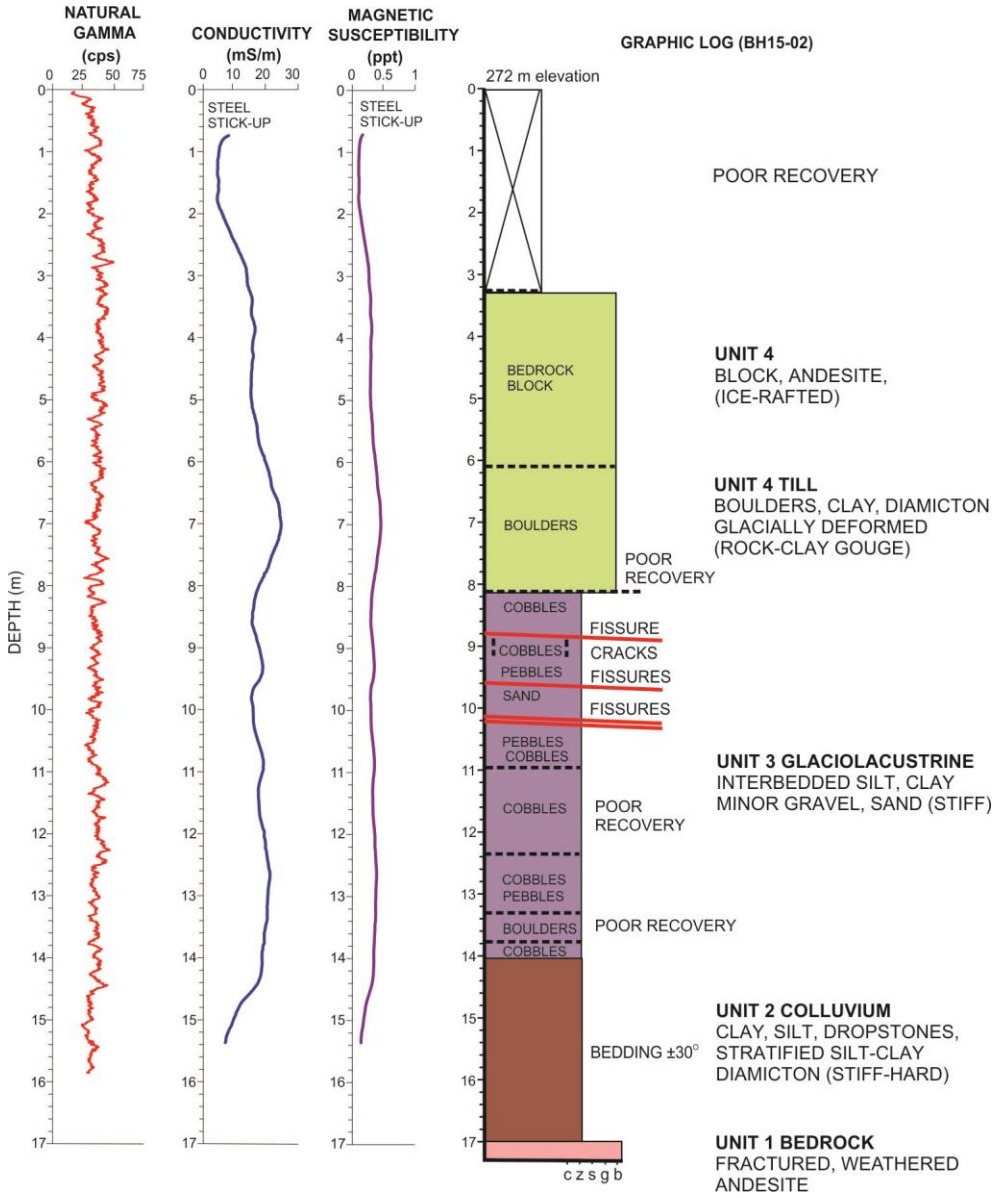

Figure 15b Natural gamma, conductivity and magnetic susceptibility results plotted and graphic log profile for BH15-02; see **Figure 2** and **Figure 6a** for location (after Gugins and Candy, 2015); grain sizes, c – clay; z – silt; s – sand; g – pebbles, cobbles; b – boulders.

Conductivity and magnetic susceptibility logs begin at the base of the steel pick-up at 0.9 m below surface (**Figure 15b**). Below this depth, the conductivity log displays a gentle increase to a depth of 7 m where it reaches a high of 26 mS m^{-1}. From 3 m to 6 m, moderate conductivity values are coincident with an interpreted ice-rafted block of andesite. This bedrock block is an analog for the buried features recorded in the terrestrial geophysical surveys. The peak in conductivity from 6 m to 8 m coincides with till diamicton and an increase in clay content in the borehole log. A minor peak in conductivity between 8.6 m and 10 m is coincident with a zone of fissures and cracks in unit 3 immediately underlying unit 4, and may indicate the presence of groundwater. These structures are slide planes or relict glaciotectonic structures. Below this

conductivity relative high, the response averages approximately 18 mS m^{-1} until 14.5 m depth where it decreases to a minimum of 8 mS m^{-1} at the bottom of the borehole. Clay, with minor amounts of silt, sand and gravel (unit 3) and diamicton containing silt, clay and pebbles (unit 2) are recorded in the borehole log over this depth interval (**Figure 15b**). The magnetic susceptibility log shows values <0.3 ppt, indicating a very low ferromagnetic mineral content in the surrounding earth materials (Gugins and Candy, 2015). The slight decrease in conductivity and MS values apparent near the base of the borehole possibly corresponds to the intersection of unconsolidated earth materials (unit 2) from 14 to 17 m depth (**Figure 15b**).

BH15-03 is located approximately 100 m from the southwest end of geophysical survey Line E, 10 m north from Line C on the east side of the CPR tracks and 100 m southwest of BH15-02 (**Figure 2**, **Figure 6a**). Again, the variation in natural gamma was generally low with a response averaging approximately 35 cps (**Figure 15c**). Minor changes in readings throughout the borehole reflect small variations in clay, and the presence of dropstones and erratic clasts. Below the steel stick-up, the conductivity log varies between 6 mS m^{-1} and 26 mS m^{-1}. The generally low conductivity throughout the entire borehole (**Figure 15c**) is consistent with BH15-01 and BH15-02, and reflects undersaturated conditions and low porosities in the subsurface glacial deposits (units 2, 3 and 4) and bedrock (unit 1). Variations in conductivity between 4.2 m and 8.8 m may be a response to higher water levels contained in glacial deformation features, sand layers, fissures, cracks and a shear zone between these depths. The decrease in response to approximately 7 mS m^{-1} observed at 14.6 m likely corresponds to a decrease in porosity in the stiff to hard clay intersected in the bottom of the borehole (Gugins and Candy, 2015). Magnetic susceptibility is consistent at about 0.28 ppt down to the onset of stiff to hard clay diamicton (unit 2) (**Figure 14c**). At about 14 m depth, the MS values decrease suggesting low concentrations of ferromagnesian minerals in the basal unit (Gugins and Candy, 2015).

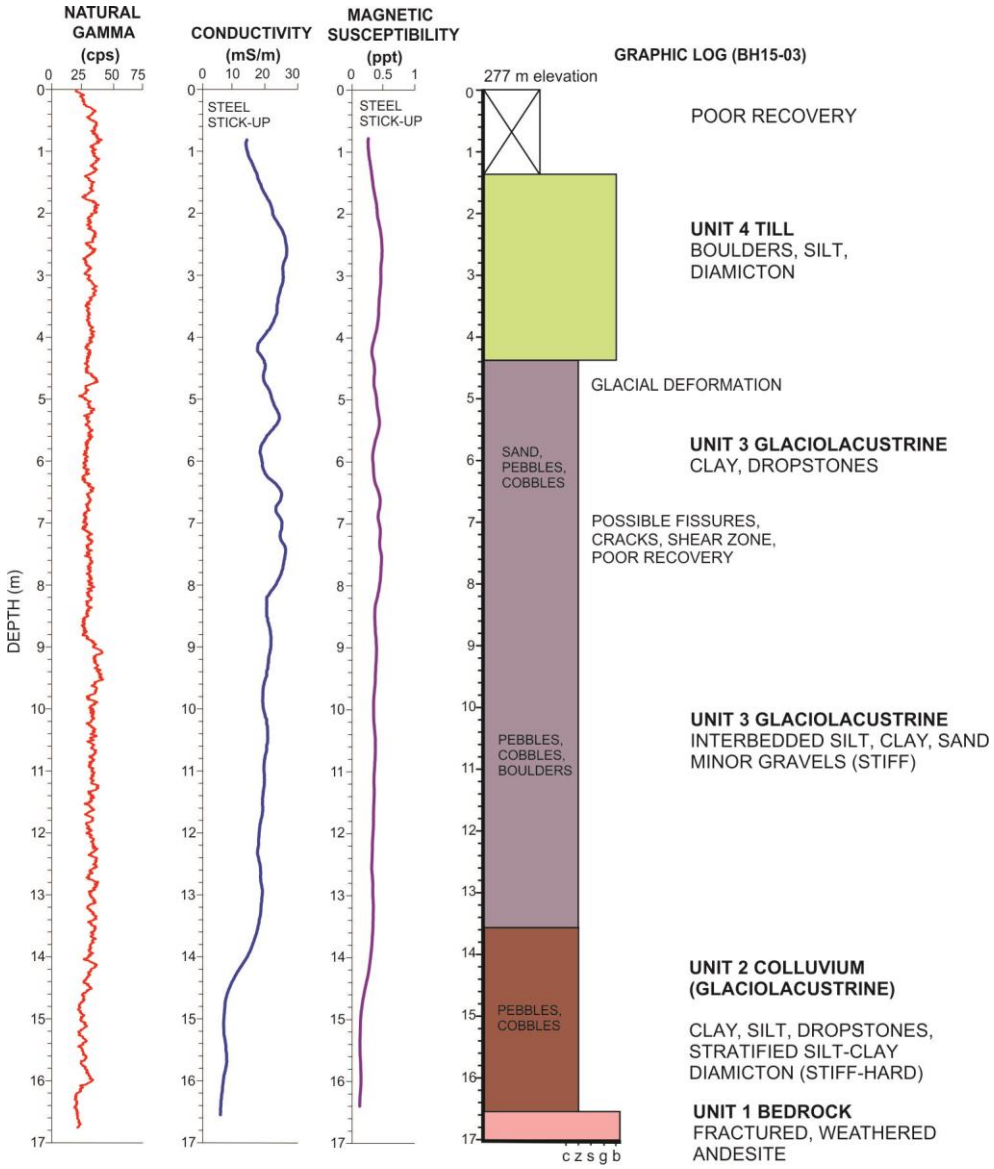

Figure 15c Natural gamma, conductivity and magnetic susceptibility results plotted and graphic log profile for BH15-03; see **Figure 2** and **Figure 6a** for location (after Gugins and Candy, 2015); grain sizes, c – clay; z – silt; s – sand; g – pebbles, cobbles; b – boulders.

6. Discussion and Summary: Addressing Knowledge Gaps

6.1 Logistics, Constraints and Limitations

The combination of working along "live" railway tracks, steep and uneven terrain and loose unconsolidated soils created challenges during the collection and processing of resultant datasets for all terrestrial geophysical techniques. Daily, between 10 to 20 trains crossed the landslide during survey hours. Both CN and CP safety protocols required that all work ceased during these times. With most trains over a couple of kilometres in length, down-time during surveys could be up to 30 minutes or more.

For T-ERT surveys, track ballast provided a challenge to electrode placement, and cables had to be laid under the train tracks. Logistically, T-FEM data were slow to collect and had significant restrictions due to the required cable lengths, topography, presence of metal fences and other loose metal on site, and safety requirements around live rail tracks. Also, T-FEM data provided little information on fine scale layering of subsurface units. T-GPR data collection was limited to areas away from the CN and CP train tracks to avoid signal feedback. The steep and loose terrain limited coupling of the antennae with surface slope. Boulder-rich clay deposits in the upper 5 m of all profiles generated pronounced reflections in an otherwise subdued datasets. The conductive clay absorbed much of the GPR signal, muting reflections from underlying units. Geophones were very sensitive to train motion, so collection of SR datasets was restricted to intervals when there was no traffic within 5 km of the landslide. Shallow buried glacial erratic boulders, loose colluvial surface deposits, and steep slopes also presented challenges to the seismic survey, partly resolved by means of careful placing of the metal plate and precision and strength of sledge hammer blows to deliver acoustic energy signals. Subsurface materials intersected by the boreholes generated subdued responses to GR, IC and MS logging.

Thompson River is very fast-flowing with significant rapids that hindered waterborne geophysical surveys using conventional watercraft and was a serious safety issue. Considerable time, effort and resources were expended in dangerous waters over two months during the 2014 waterborne survey using a piloted jet boat and white-water raft. The long W-ERT array did not allow traverses of the river perpendicular to flow because the channel was less than 100 m wide and the array trailed downstream in the very strong currents. As a result, cross-river lines planned to extend from existing land cross-section lines out into the river were not surveyed.

6.2 Outcome of Multi-Technique Approach

An unprecedented level of insight into the internal composition and structure of the very slow-moving Ripley Landslide has been gained by combining the results of terrestrial, waterborne and borehole geophysical surveys and discussing these datasets in the context of ground observations, surficial geology mapping and instrumental monitoring. For this study, waterborne and terrestrial Electrical Resistivity Tomography (ERT), Fixed Frequency-Domain Electromagnetic Induction (FEM), Ground Penetrating Radar (GPR), Seismic Refraction (SR) and Multispectral Analysis of Shear Wave (MASW) surveys were combined with down-hole measurement of natural Gamma Readings (GR), Induction Conductivity (IC) and Magnetic Susceptibility (MS).

T-ERT and W-ERT data provided the most complete information regarding the internal structure of the landslide and, except for the terrestrial seismic data (SR and MASW), provides deeper information than the other techniques. Although SR and MASW data provide information at depth, the detail is less than the T-ERT (and W-ERT) data. T-FEM and W-EM31 data only imaged the upper 10 m, but were consistent with the T-ERT and W-ERT data and added additional and useful information of the near surface resistivity/conductivity distribution. The W-EM data shows potential locations of groundwater discharge. T-GPR and W-GPR data showed interesting results but there are difficulties in interpretation due to the presence of a number of diffracting centres, mostly boulders at various depths.

6.3 Landslide Geophysical Model

Similar to other slides in the Thompson River valley, channel incision, falling river discharge and low groundwater levels in the winter months significantly affect toe slope stability and mobility of the Ripley Landslide. All monitoring techniques confirm movement across the main slide body. This is where surficial mapping, boreholes and geophysical surveys indicate a high relief bedrock surface overlain by a >20 m thick package of till diamicton (unit 4), silt, clay and diamicton (units 2 and 3) and groundwater-rich bedrock (unit 1) that extends under the river. Planar physical sub-surface features revealed in field observations and borehole logs include tabular bedding and terrain unit contacts, in addition to curvilinear-rectilinear features interpreted as sub-vertical tension cracks and sub-horizontal rotational-translational slide planes in clay-rich beds beneath the rail ballast and retaining wall at depths between 5 m and 15 m below the surface of the main landslide body. Geophysical profiles show that the surficial units most likely contain failure planes are glaciolacustrine clay beds (units 2 and 3) and till diamicton (unit 4). Above these translational slide surfaces, glacial deposits (units 2 to 7), postglacial colluvium (unit 8) and alluvial sediments (unit 9), together with rail ballast and the lock-block retaining wall (unit 10) move downslope as relatively coherent blocks toward the river (**Figure 16** and **Figure 17**).

Small and irregular anomalies, areas of complex subsurface geometry and groundwater-rich zones are resolved along all terrestrial geophysical survey lines. Non-porous, fractured, weathered magnetite- and ilmenite-bearing andesite, rhyolite and pyroclastic rocks (unit 1) and coarse, rapidly drained ballast (unit 10), alluvium (unit 9) and colluvium (unit 8) have high apparent resistivity values in T-ERT and T-FEM profiles (**Table 2**; **Figure 7**; **Figure 8**). Till diamicton (unit 4), glaciofluvial gravel outwash (unit 6) and colluviated clay and bedrock at depth (unit 2) are moderately resistive (**Table 2**). Areas with low resistivity values include clay-silt units (units 2 and 3, **Table 2**), deposits or landslide structures containing groundwater. T-ERT data provide an indication of possible up-slope moisture migration paths in the vicinity of steep gullies. The data also appear to image rafted bedrock at depth. This would indicate glacial transport and erosion or past landslide activity involving large rock masses. The depths and locations of this block are somewhat out of alignment in **Figures 7a** and **7b** because RES2DINV assumes a two dimensional structure, while the block has three.

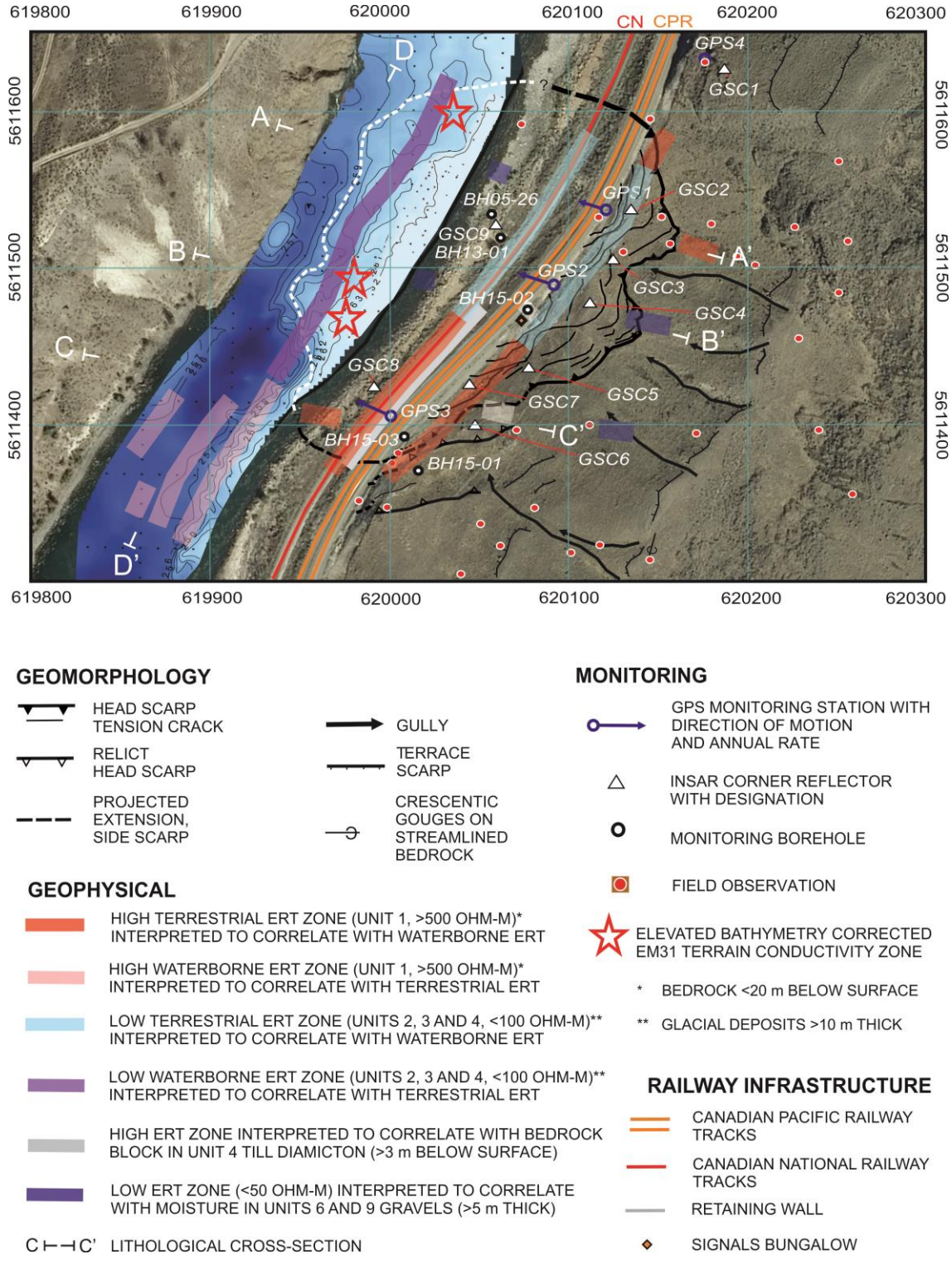

Figure 16 Summary of key geophysical features from ERT, FEM, GPR, seismic and borehole surveys (after Bunce and Chadwick, 2012; Huntley and Bobrowsky, 2014; Parry et al., 2014; Bauman et al., 2015; Gugins and Candy, 2015); A-A', B-B', C-C' and D-D' – lithological cross-sections (see **Figure 17**).

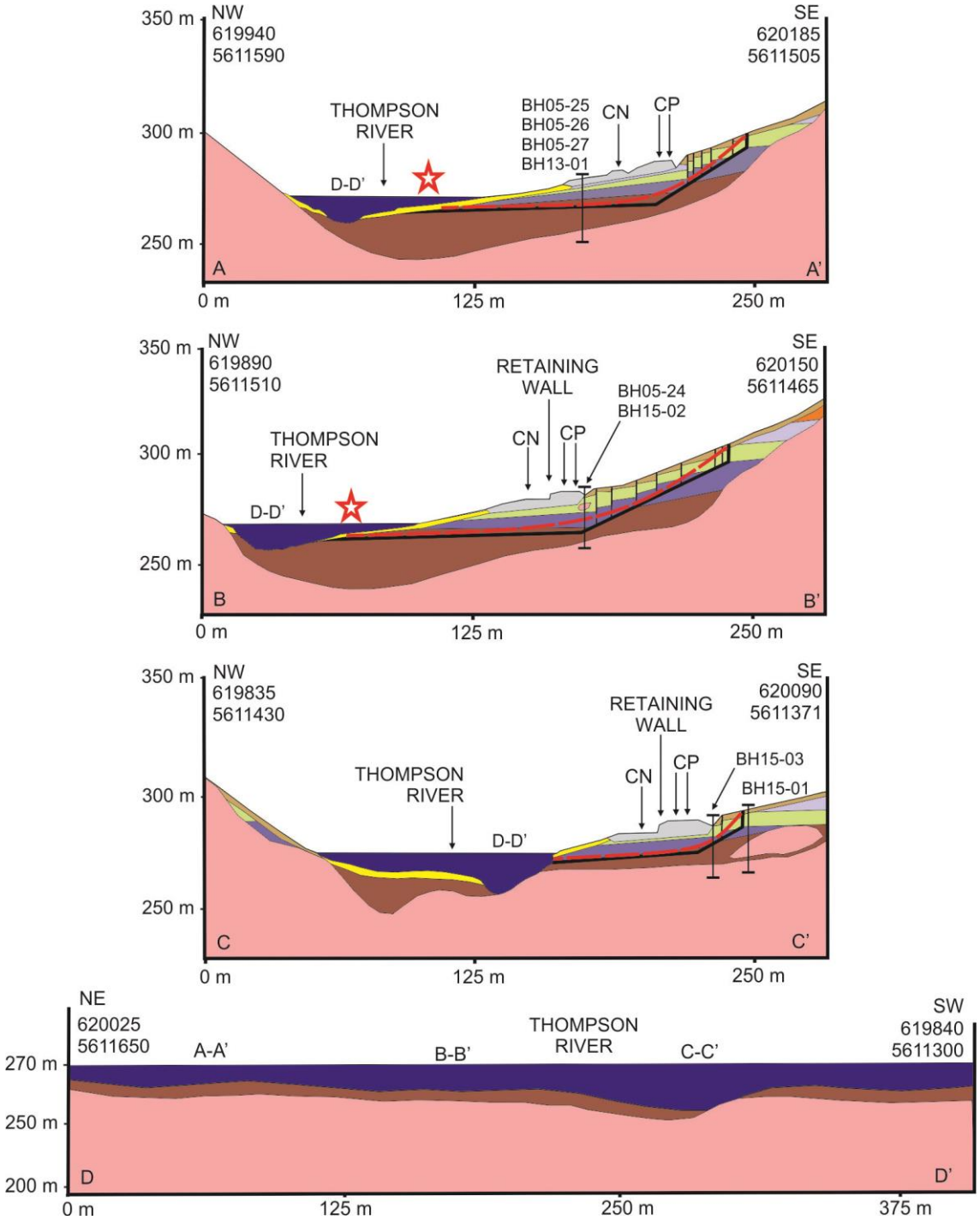

Figure 17 Interpretation of stratigraphy and landslide structures along cross-sections A-A', B-B', C-C' and D-D' based on results discussed in this report. See **Figure 2** for earth material legend. Two solutions are shown for the geometry of the failure zone(s): rectilinear (translational) failure planes - solid black lines; curvilinear (translational-rotational) – dashed red lines. Locations of boreholes Elevated waterborne EM34 terrain conductivity zones indicated with red stars.

Subdued reflectors in T-GPR profiles likely correspond to different units at depths less than 20 m and indicate slight contrasts between clay, silt (units 3 and 5), coarser diamictons (units 2 and 4), bedrock (unit 1), and groundwater-saturated earth materials (**Figure 9**). Seismic refraction and MASW data predominantly reflect the consolidation and earth material density (**Figure 10**). Since fine lithological layering is not evident in the seismic data from the refraction analysis, earth materials have largely been inferred by physical location along the seismic profile rather than by acoustic velocity. At depth, boulder and clay-rich colluvium, glaciolacustrine clays and till are hard to stiff, producing higher P-wave velocities than expected. Further analysis and re-evaluation of the P-wave data is suggested, incorporating knowledge of geotechnical properties and local stratigraphy as revealed in borehole logging across the landslide. Seismic refraction lines A and C have a relatively steep velocity gradient in the deeper part of the profiles in comparison to SR Line B, reflecting the subsurface bedrock relief. A hidden seismic low velocity layer in the upper 20 m on SR Line C upslope of the CPR and CN rail tracks, also recorded in the T-ERT and T-GPR data, is interpreted as a buried rafted bedrock block and warrants further investigation to understand the dynamics of the different sub-surface layers that exist there. A similar bedrock raft within unit 4 is recorded in BH15-02 at 3 m to 5 m below the surface (**Figure 15**).

The MASW results for seismic lines A to E illustrate a general increase in velocity with depth (**Figure 10**; Gugins and Candy, 2015). The areas of thick glacial deposits (>10 m) located at lower elevations and over the western half of the site area are clearly delineated by lower shear wave velocities. Along MASW lines D and E, a surface to near-surface low shear wave velocity layer, with an average 10 m thickness, corresponds to borehole intersections of silt and clay diamicton containing glacially-transported granitic boulders and locally-derived, rafted andesite blocks (unit 4, **Table 2**). This layer is interpreted to represent the earth materials contained in the main body of the landslide. Underlying the low velocity layer, shear wave velocities increase from, corresponding to the onset of denser stiff to hard clay, silt and sand, and stiff clay (unit 3, **Table 2**) recorded at depth in borehole logs (**Figure 15**). Beneath this dense layer, the shear wave velocities increase, consistent with borehole intersections of andesite bedrock (unit 1, **Table 2**).

Natural GR logs show a relatively constant response interpreted to indicate the predominance of clay in the glacial deposits. Minor changes in readings throughout the borehole are interpreted to reflect small variations in clay, silt and sand content (in units 2 and 3), and the presence of granitic and arkosic dropstones (units 2 and 3) and erratics (in unit 4) immediately adjacent to boreholes. The IC logs show a progressive, but subtle rise corresponding to an increase in clay content with depth (**Table 2**, **Figure 15**). High conductivity zones indicate clay horizons in silt- and boulder-rich till (unit 4) or an increase in water content along fissures, fractures, cracks and shear planes (**Figure 15**). At depth, conductivity values fall in response to a porosity decrease in stiff to hard silt-clay diamicton (unit 2) and electrically resistive andesite intersected in the bottom of boreholes (unit 1). Magnetic susceptibility logs show a consistent low response, indicating a very low ferromagnetic mineral content in the surrounding glacial deposits (units 2, 3 and 4). Although strong contrasts in the T-ERT and T-FEM data are observed at the boundary of units 1 and 2 at a much larger scale, there is little variation between the bedrock and the overlying clay-

rich beds recorded in the IC and MS logs (**Table 2**; **Figure 15**). This suggests the upper meter of bedrock is fractured, weathered and intermixed with overlying material. Had the boreholes penetrated deeper into non-weathered andesite, an increase in IC and MS levels would be anticipated.

Waterborne bathymetric and geophysical surveys indicate the landslide extends under the Thompson River, where >20 m of sediment is confined to a bedrock basin (**Figure 12**). Data acquired along W-ERT lines 2 and 3 have delineated a layer of high resistivity beneath the Thompson River that correlates with a high T-ERT zone in the southwestern portion of the landslide with correspondingly high P-wave and shear wave velocities (**Table 2**; **Figure 3**, lines C, D and E; **Figure 16**). This sub-river layer has been interpreted to be unit 1, bedrock (**Table 2**; **Figure 10**). To the northeast, W-GPR and W-ERT data show a 20 m thick low resistivity layer overlying bedrock, interpreted to be clay, silt and diamicton with interstitial boulders (units 2, 3 and 4) (**Table 2**; **Figure 12**; **Figure 14**). Alternatively, or in combination, the low resistivity values could be attributed to the presence of groundwater within the submerged portion of the landslide. Bathymetry corrected W-EM31 data have delineated three zones of relatively elevated terrain conductivity that perhaps indicate discharge of groundwater at the landslide toe (**Figure 13; Figure 16**; **Figure 17**). Waterborne GPR data show no obvious stratigraphy or layering, but display multiple diffractions interpreted as erratic boulders in units 2, 3 and 4, colluvial blocks (unit 8), and a lag deposit of modern fluvial boulders (unit 9) (**Figure 14**). Underlying units are armoured from erosion by this lag deposit except where a deep trough and scour pool is carved by strong currents (**Figure 11**; **Figure 14**). Toe slope incision is occurring adjacent to where the highest ground motion rates are recorded on the landslide, and where critical railway infrastructure is at risk.

6.4 Recommendations for Future Work and Summary

The geophysical datasets presented and discussed here provide new insights into subsurface glacial deposits and deformation structures that are contributing to displacement across the main landslide body, in the rail ballast, and in the retaining wall separating the CN and CPR tracks. Surficial mapping and geophysical survey data indicate a high relief bedrock surface overlain by a >20 m thick package of till diamicton (unit 4), silt, clay and diamicton (units 2 and 3) and groundwater-rich bedrock (unit 1). Active translational failure planes between 5 m and 15 m depth are restricted to glaciolacustrine clay beds (units 2 and 3) beneath the main slide body, rail ballast and lock-block retaining retaining wall (**Figure 17**).

A remaining objective for the geophysical survey is to extend T-ERT lines B and C across the Thompson River in low flow conditions (i.e., during the winter months). Since the Thompson River does not freeze over, the safest and most cost-effective option to complete the remaining W-ERT lines would be to deploy an unmanned aquatic vessel (UAV) at the lowest stage of river flow during the winter to reduce noise from rapids and very strong currents. High density bathymetry, W-ERT and other data acquired by this mobile platform would refine the interpretations presented in this paper and results from other monitoring programs. Processing steps applied to the GPR data were basic and further processing may bring out additional features.

More aggressive band passes, background filtering and different gain functions could be applied to emphasise either shallow or deep, dipping or horizontal reflectors. Multi-fold GPR data would allow stacking and improved resolution of the reflections currently seen and other layers that are currently unresolvable due to signal-to-noise levels.

The combination of data from surficial geology mapping and the array of geophysical techniques employed in this study provided significantly more information than any one method on its own. This information provides the physical context for understanding results from other monitoring programs underway (e.g., Bobrowsky et al., 2014; Huntley et al., 2014; Macciotta et al., 2014; Hendry et al., 2015; Schafer et al. 2015). Effective landslide monitoring will help ensure the safety and security of critical railway transportation infrastructure, thereby reducing risks to public safety, the environment, natural resources and economy of Canada and elsewhere.

7. Acknowledgements

GSC Open File 8062 greatly benefitted from a critical review by Heather Crow (GSC Ottawa). We wish to thank Megan Caston, Cassandra Budd and Gordon Brasnett (Tetra Tech EBA Inc., Edmonton, Alberta) for their geophysical services in 2013-2014; Landon Woods and Kimberly Hume (Advisian, Worley Parsons Group, Calgary, Alberta) in 2014-2015; and Caitlin Gugins and Heather Ainsworth (Frontier Geosciences Inc., North Vancouver, British Columbia) in 2015. The project benefited from management by Carmel Lowe, Adrienne Jones, Philip Hill (GSC Sidney, British Columbia), Andrée Blais-Stevens (GSC Ottawa); and Sharon Philpott and Merrina Zhang (Transport Canada, Ottawa, Ontario). Coordination of the Railway Ground Hazard Research Program was managed by Cindy Hick (HPB Association Management, Ottawa, Ontario). The following colleagues contributed on site and in the office, and ensured researchers operated in safety: Wendy Sladen and Baolin Wang (GSC Ottawa, Ontario), Lionel Jackson (GSC Vancouver, British Columbia), Erin Dlabola (GSC Sidney), Laura Weise (GSC International Intern, University of Potsdam, Germany); Karolin Doeringer Weise (GSC International Intern, University of Vienna, Austria); Zhang Qing, Zhang Xiaofei and Lv Zhonghu (Centre for Hydrogeology and Environmental Geology, China Geological Survey, Baoding, China); Hengxing Lan (Chinese Academy of Sciences, Beijing, China); Michael Hendry, Derek Martin, Renato Macciotta, Matthew Schafer, Gael Le Meil, Jeff Journault and Kristen Tappenden (University of Alberta, Civil and Environmental Engineering, Edmonton, Alberta); and from 2013 to 2015, Chris Bunce, Eddie Choi, Gary Maximiuk, Roy Olsen and Matt Rhoades (Canadian Pacific Railway); Tom Edwards, Jennifer Kutchner and Mark McKay (Canadian National Railway); and Ian Chadwick (ERD Consulting Ltd., Kamloops, British Columbia).

8. References

Bauman, P., Woods, L. and Hume, K. (2015) 2014 Geophysical Investigation at the Ripley Landslide, Thompson River Valley, South of Ashcroft, B.C. Worley Parsons Canada, Unpublished Report for the Geological Survey of Canada, Project 307074-02008, 15 pages, 17 figures, 6 photographs and 1 appendix

Best, M., Bobrowsky, P., Douma, M., Carlotto, V. and Pari, W. (2009) Geophysical surveys at Macchu Picchu, Peru: results for Landslide Hazards Investigations. *In* K. Sassa and P. Canuti (Editors), Landslides – Disaster Risk Reduction, pp. 265-273, Springer-Verlag

BGC Engineering Inc. (2005) Project: THOM 52.80 Westcap Geotechnical Investigations. Unpublished geotechnical logs, Canadian Pacific Railway

BGC Engineering Inc. (2013) Project: Ripley Instrumentation. Unpublished geotechnical logs, Canadian National Railway

Bichler, A., Bobrowsky, P., Best, M., Douma, M., Hunter, J., Calvert, T. and R. Burns (2004) Three-dimensional mapping of a landslide using a multi-geophysical approach: the Quesnel Forks landslide. Landslides, Vol. 1, No. 1, p. 29-40. DOI: 10.1007/s10346-003-0008-7 (Contribution #2005492)

Bishop, N., Evans, S., Petley, D. and Unger, A. (2008) The geotechnics of glaciolacustrine sediments and associated landslides near Ashcroft (British Columbia) and the Grand Coulee Dam (Washington). *In* Proceedings of the 4th Canadian Conference on Geohazards: From Causes to Management, 594 p.

Bobrowsky, P.T., Sladen, W., Huntley, D., Zhang, Q., Bunce, C., Edwards, T., Hendry, M., Martin, D. and E. Choi (2014) Multi-parameter monitoring of a slow moving landslide: Ripley Slide, British Columbia, Canada. In: Engineering Geology for Society and Territory – Volume 2 Landslide Processes, edited by G. Lollino, D. Giordan, G. Battista Crosta, J. Corominas, R. Azzam, J. Wasowski and N. Sciarra; p. 155-159. IAEG (International Association of Engineering Geology and the Environment) Congress, Turin, Italy 15 – 19 September 2014, Springer Publishing (Contribution #20140007)

Bunce, C. and Chadwick, I. (2012) GPS monitoring of a landslide for railways. *In* Eberhardt et al. (Editors), Landslides and Engineered Slopes: Protecting Society through Improved Understanding, pp. 1373-1379

Butler, E.B., Nadeau, J.C., Parrott, R. and Daigle, A. (2004) Delineating recharge to a river valley aquifer by riverine seismic and EM methods. Journal of Environmental and Engineering Geophysics, Volume 9, pp. 95-109

Clague, J. and Evans, S. (2003) Geologic framework for large historic landslides in Thompson River valley, British Columbia. Environmental and Engineering Geoscience, Vol. IX, pp. 201-212

Davis, J.L. and Annan, A.P. (1989) Ground penetrating radar for high resolution mapping of soil and rock stratigraphy. Geophysical Prospecting, Vol. 37, pp. 531-551

Eshraghian, A., Martin, D. and Cruden, D. (2007) Complex earth slides in the Thompson River Valley, Ashcroft, British Columbia. Environmental and Engineering Geoscience, Vol. XIII, pp. 161-181

Eshraghian, A., Martin, D. and Morgenstern, N. (2008) Movement triggers and mechanisms of two earth slides in the Thompson River Valley, British Columbia, Canada. Canadian Geotechnical Journal, Vol. 45, pp. 1189-1209

Fulton, R.J. (1969) Glacial lake history, southern Interior Plateau, British Columbia. Geological Survey of Canada Paper 69-37, 14 p.

Geotomo (2012) RES2DINV: a rapid 2-D resistivity & IP inversion using the least-squares method, Geoelectrical Imaging 2D & 3D Geotomo Software, Penang, Malaysia, www.geotomosoft.com

Gugins, C. and Candy, C. (2015) Downhole logging and multi-spectral analysis of surface waves (MASW) investigation, Ripley Landslide Project, Ashcroft area, B.C. Frontier Geosciences Inc. Unpublished Report for the Geological Survey of Canada, Project FGI-1390, 12 p.

Hendry, M., Macciotta, R. and Martin, D. (2015) Effect of Thompson River elevation on velocity and instability of Ripley Slide. Canadian Geotechnical Journal, Vol. 52(3), pp. 257-267

Huntley, D. and Bobrowsky, P. (2014) Surficial geology and monitoring of the Ripley Slide, near Ashcroft, British Columbia, Canada; Geological Survey of Canada, Open File 7531, 21 p.

Huntley, D., Bobrowsky, P., Qing, Z., Sladen, W., Bunce, C., Edwards, T., Hendry, M., Martin, D. and E. Choi (2014) Fiber optic strain monitoring and evaluation of a slow-moving landslide near Ashcroft, British Columbia, Canada. In: Landslide Science for a Safer Geoenvironment, edited by K. Sassa, P. Canuti and Y. Yin, Volume 1, p. 415-422. Springer Verlag. 3rd World Landslide Forum (ICL-IPL), Beijing, China 2 – 6 June 2014. (Contribution #20150019)

Johnsen, T. and Brennand, T. (2004) Late-glacial lakes in the Thompson Basin, British Columbia: paleogeography and evolution. Canadian Journal of Earth Sciences, Vol. 41. pp. 1367-1383.

Macciotta, R., Hendry, M., Martin, D., Elwood, D, Lan, H., Huntley, D., Bobrowsky, P. , Sladen, W, Bunce C., Choi, E and Edwards, T. (2014) Monitoring of the Ripley Slide in the Thompson River Valley, B.C. Proceedings of Geohazards 6 Symposium, Kingston, Ontario, Canada

McNeill, J. (1980a) Technical Note TN-5 Electrical Conductivity of Soils and Rocks, Geonics Ltd.

McNeill, J. (1980b) Technical Note TN-6 Electromagnetic Terrain Conductivity Measurement at Low Induction Numbers, Geonics Ltd.

McNeill JD, 1986. Geonics-EM39 borehole conductivity meter, theory of operation; Geonics Technical Note TN-20, Geonics Ltd.

Monger, J. (1985) Structural evolution of the southwestern Intermontane belt, Ashcroft and Hope map areas, British Columbia. *In* Current Research, Part A, Geological Survey of Canada, Paper 85-1A, pp. 349-358.

Monger, J. and McMillan, W. (1984) Bedrock geology of Ashcroft (92I) map area. Geological Survey of Canada, Open File 980, scale 1:250,000

Morey, R. (1974) Continuous Subsurface Profiling by Impulse Radar, In Proceedings of Engineering Foundation Conference on Subsurface Exploration for Underground Excavation and Heavy Construction, American Society of Civil Engineers, pp. 213-232, Henniker, New Hampshire. New York:

Mortimer, N. (1987) The Nicola Group: Late Triassic and Early Jurassic subduction-related volcanism in British Columbia. Canadian Journal of Earth Sciences, Vol. 24, pp. 2521-2536

Noon, D., Longstaff, D. and Yelf, R. (1994) Advances in the Development of Step Frequency Ground Penetrating Radar, In Proceedings of the 5th International Conference on Ground Penetrating Radar, Vol. I, pp 117-131, Kitchener, Ontario, Canada

Parry, N., Caston, M., Budd, C. and Brasnett, G. (2014) Geophysical data collection: Electrical Resistivity Tomography, Fixed Frequency Electromagnetic Induction, Ground Penetrating Radar and Seismic Refraction; Ripley Slide, near Ashcroft, BC., TetraTech EBA, Unpublished Report for the Geological Survey of Canada, File: 704-E11103058

Porter, M., Savigny, K., Keegan, T., Bunce, C. and MacKay, C. (2002) Controls on stability of the Thompson River landslides. *In* Proceedings of the 55th Canadian Geotechnical Conference: Ground and Water – Theory to Practice, Canadian Geotechnical Society, pp. 1393-1400

Ryder, J. (1976) Surficial geology, Ashcroft, British Columbia. Geological Survey of Canada, A-Series Map 1405A, scale 1:126,720

Ryder, J., Fulton, R. and Clague, J. (1991) The Cordilleran Ice Sheet and the glacial geomorphology of southern and central British Columbia. Géographie physique et Quaternaire, Vol. 45, pp. 365-377

Sandmeier, K. (1998-2012) REFLEXW Version 7.0 Manual, pp. 509-519

Schafer, M., Macciotta, R., Hendry, M., Martin, D., Bobrowsky, P., Huntley, D., Bunce, C. and Edwards, T. (2015) Instrumenting and Monitoring a Slow Moving Landslide. GeoQuebec 2015 Paper, 7 p.

Tribe, S. (2005) Eocene paleo-physiography and drainage directions, southern Interior Plateau, British Columbia. Canadian Journal of Earth Sciences, Vol. 42, pp. 215-230

Ulruksen, C.P.F. (1982) Application of Impulse Radar to Civil Engineering, Unpublished PhD. Thesis, Department of Engineering Geology, University of Technology, Lund, Sweden

Yilmaz, Ö. (2001) Seismic Data Analysis Processing, Inversion, and Interpretation of Seismic Data, *In* Doherty, S.M. (Editors), SEG Investigations in Geophysics, No. 10, Vol. 1, Ch. 3.4